Check for updates

AGU ADVANCING EARTH AND SPACE SCIENCE

Water Resources Research

RESEARCH ARTICLE
10.1029/2021WR031147

Disconnected Gas Transport in Steady-State Three-Phase Flow

Abdulla Alhosani[1], Ahmed M. Selem[1], Qingyang Lin[2], Branko Bijeljic[1], and Martin J. Blunt[1,3]

[1]Department of Earth Science and Engineering, Imperial College London, London, UK, [2]State Environmental Protection Engineering Center for Coal-Fired Air Pollution Control, State Key Laboratory of Clean Energy Utilization, Zhejiang University, Hangzhou, China, [3]Department of Energy, Politecnico di Milano, Milan, Italy

Key Points:

- Gas flow is disconnected at steady-state conditions, explaining the low gas relative permeability seen in this water-wet three-phase system
- Intermittent gas-oil flow is observed in intermediate-sized pores despite flowing at low flowrates, where capillary forces are dominant
- The traditional use of two-phase data to predict three-phase flow vastly over-estimates the connectivity and mobility of the gas phase

Supporting Information:

Supporting Information may be found in the online version of this article.

Correspondence to:

A. Alhosani,
Abdulla.alhosani17@imperial.ac.uk

Citation:

Alhosani, A., Selem, A. M., Lin, Q., Bijeljic, B., & Blunt, M. J. (2021). Disconnected gas transport in steady-state three-phase flow. *Water Resources Research*, *57*, e2021WR031147. https://doi.org/10.1029/2021WR031147

Received 3 SEP 2021
Accepted 21 NOV 2021

Author Contributions:

Conceptualization: Abdulla Alhosani, Branko Bijeljic, Martin J. Blunt
Data curation: Abdulla Alhosani, Qingyang Lin
Formal analysis: Abdulla Alhosani, Qingyang Lin, Martin J. Blunt
Funding acquisition: Martin J. Blunt
Investigation: Abdulla Alhosani, Ahmed M. Selem, Qingyang Lin, Branko Bijeljic, Martin J. Blunt
Methodology: Abdulla Alhosani, Qingyang Lin, Branko Bijeljic, Martin J. Blunt
Resources: Abdulla Alhosani
Software: Abdulla Alhosani, Qingyang Lin

© 2021. The Authors.
This is an open access article under the terms of the Creative Commons Attribution License, which permits use, distribution and reproduction in any medium, provided the original work is properly cited.

Abstract We use high-resolution three-dimensional X-ray microtomography to investigate fluid displacement during steady-state three-phase flow in a cm-sized water-wet sandstone rock sample. The pressure differential across the sample is measured which enables the determination of relative permeability; capillary pressure is also estimated from the interfacial curvature. Though the measured relative permeabilities are consistent, to within experimental uncertainty, with values obtained without imaging on larger samples, we discover a unique flow dynamics. The most non-wetting phase (gas) is disconnected across the system: gas flows by periodically opening critical flow pathways in intermediate-sized pores. While this phenomenon has been observed in two-phase flow, here it is significant at low flow rates, where capillary forces dominate at the pore-scale. Gas movement proceeds in a series of double and multiple displacement events. Implications for the design of three-phase flow processes and current empirical models are discussed: the traditional conceptualization of three-phase dynamics based on analogies to two-phase flow vastly over-estimates the connectivity and flow potential of the gas phase.

1. Introduction

The empirical extension of Darcy's law for flow in a porous medium to multiple phases proposed 85 years ago implicitly assumes that each phase flows, in steady-state, through a fixed subset of the pore space, and explicitly states that there is a linear relationship between pressure gradient and flow rate (the Darcy flux of each phase) (Wyckoff & Botset, 1936). While for two-phase flow it is now well-established that a non-linear relationship between rate and pressure gradient emerges for fast flows, there is still a linear Darcy-like regime for capillary-controlled displacement, which is seen in most natural and engineered settings, where the fluids indeed flow through fixed pathways (Gao et al., 2017; Gjennestad et al., 2020; Reynolds et al., 2017). Therefore, the presumption is that in three-phase flow again there would be a capillary-dominated flow regime with fixed flow paths.

In this paper, we show that this is not the case and that three-phase flow appears to have a unique dynamics; even for capillary-controlled flow, the most non-wetting phase (gas in our experiments) is always disconnected across the system and is transported through the intermittent opening and closing of critical flow paths. This is facilitated by double and multiple displacement events, which are a unique feature of three-phase flow (Øren et al., 1992; Sohrabi et al., 2004; Sorbie & van Dijke, 2010; van Dijke & Sorbie, 2002).

Quantifying three-phase flow is essential for the design of reservoir models that simulate the behavior of gas, oil and water in geological systems (Blunt, 2017; Oak, 1990). These models help make operational decisions for many subsurface applications including carbon capture and storage (CCS) (Bickle, 2009; Kramer, 2020; Stewart et al., 2018), nonaqueous phase liquid (NAPL) pollutant removal (Descorme, 2017; Mayer & Miller, 1993), and enhanced oil recovery (EOR) processes (Abdulkareem & Padmanabhan, 2021; Blunt et al., 1993; Lake, 1989). At present, relative permeability, the saturation-dependent factor by which flow conductance is reduced in multiphase flow, can either be measured experimentally or predicted empirically (Blunt, 2017). However, our empirical models are currently incapable of predicting three-phase relative permeability to within an acceptable accuracy in many circumstances (Alizadeh & Piri, 2014b). This is mainly attributed to the lack of understanding of the impact of complex pore-scale processes that occur during three-phase flow, namely wettability, layer flow, multiple displacements, and saturation history, on relative permeability. Indeed, as stated above, it is not even evident that a Darcy-like law to describe the flow is valid at all.

The steady-state method is considered to be the most reliable approach to measure relative permeability since it directly uses the multiphase Darcy law (Alizadeh & Piri, 2014b; Honarpour et al., 1986). Here, the fluids are

Supervision: Branko Bijeljic, Martin J. Blunt
Validation: Abdulla Alhosani
Visualization: Abdulla Alhosani, Ahmed M. Selem
Writing – original draft: Abdulla Alhosani
Writing – review & editing: Abdulla Alhosani, Ahmed M. Selem, Qingyang Lin, Branko Bijeljic, Martin J. Blunt

simultaneously injected into the rock at a set of fixed fractional flows and the differential pressure drop and saturations are recorded when steady-state conditions are reached (Honarpour et al., 1986). Nevertheless, laboratory measurements of three-phase relative permeability are complicated, expensive and time consuming. Therefore, rather than only relying on experimental measurements of macroscopic properties, we need to improve our models through a comprehensive analysis of the relationship between relative permeability and the underlying pore-scale phenomena. To do so, in this work, we develop a novel approach that combines the steady-state three-phase relative permeability measurement method with pore-scale X-ray imaging techniques.

In recent years, three-dimensional X-ray microtomography (micro-CT) has emerged as an attractive tool for studying multiphase flow processes in porous media (Blunt et al., 2013; Cnudde & Boone, 2013; Wildenschild & Sheppard, 2013). This non-invasive technology offers the advantage of visualizing the pore space and the fluids within it, providing valuable information on the fluid configuration and arrangement as well as saturation. Early work using X-ray imaging focused on investigating unsteady-state two-phase displacements which helped in assessing trapping and recovery efficiency for CO_2 storage and oil recovery applications (Alhammadi et al., 2017; Alhosani, Scanziani, Lin, Foroughi, et al., 2020; Andrew et al., 2014b, 2014c; Armstrong et al., 2012; Berg et al., 2013; Herring et al., 2017; Singh et al., 2016, 2017). The scope of the tool was then extended to study steady-state two-phase flow which enabled the simultaneous determination of relative permeability with capillary pressure in water-wet, oil-wet and mixed-wet rocks (Alhammadi et al., 2020; Gao et al., 2017, 2019; Gao, Raeini, et al., 2020; Lin et al., 2018; Zou et al., 2018). The pore-scale insights gained from combining steady-state two-phase flow with pore-scale imaging have led to significant breakthroughs in the field, explaining the relative contribution of trapped phases, layers and micro-porosity to two-phase flow mechanisms, which helped in interpreting core-scale two-phase relative permeability data (Alhammadi et al., 2020; Gao, Raeini, et al., 2020).

In contrast, the use of pore-scale X-ray imaging in three-phase flow studies has been limited to unsteady-state experiments (Alhosani, Lin, et al., 2021; Alhosani et al., 2019; Alhosani, Scanziani, Lin, Raeini, et al., 2020; Alhosani, Scanziani, Lin, Selem, et al., 2020; Feali et al., 2012; Iglauer et al., 2019; Qin et al., 2019; Scanziani, Alhammadi, et al., 2018; Scanziani, Alhosani, et al., 2020; Scanziani, Lin, et al., 2020; Scanziani, Singh, et al., 2018; Scanziani et al., 2019); to date, there is not a single experiment that combines three-phase steady-state flow with pore-scale imaging. This is solely ascribed to the practical complications of the experiment as we will discuss later. Alhosani, Bijeljic, and Blunt (2021) provide a synthesized review of unsteady-state three-phase pore-scale imaging studies. They highlight the recent insights gained on the pore-scale processes that control three-phase flow, with a particular focus on the impact of surface wettability and gas-oil miscibility on wettability order, double displacements, and trapping. To this end, we believe that developing an approach that combines three-phase steady-state flow with pore-scale imaging, where both relative permeability and capillary pressure can be measured simultaneously, as applied in two-phase flow (Gao et al., 2017; Lin et al., 2018), can ultimately aid in the development of rigorously validated, physically based pore-scale models and empirical correlations to predict three-phase relative permeabilities under various wettability and miscibility conditions.

Furthermore, pore-scale imaging can provide solutions to some of the challenges often faced during steady-state three-phase relative permeability measurements. With X-ray imaging, surface wettability can be directly assessed, especially to differentiate between weakly oil-wet and strongly oil-wet systems (Alhosani, Lin, et al., 2021; Alhosani, Scanziani, Lin, Raeini, et al., 2020; Alhosani, Scanziani, Lin, Selem, et al., 2020; Blunt et al., 2021). Pore-scale imaging can also confirm in situ the existence of spreading layers, rather than relying on an empirical relationship between the interfacial tensions to determine whether or not a phase will spread (Feali et al., 2012; Scanziani, Singh, et al., 2018). The use of imaging can help overcome a major drawback of the steady-state approach, which is the capillary end effect, by providing a direct assessment of the saturation profile along the sample (Lin et al., 2018). This can help identify and/or eliminate the regions influenced by boundary effects, increasing the accuracy and reliability of steady-state relative permeability results.

We will study three-phase flow in a water-wet porous medium. This system is well defined in the literature, with an unambiguous wettability order: water, most-wetting, resides in the smallest pores and wetting layers, gas, most non-wetting, occupies the biggest pores, while oil, intermediate-wet, spreads in layers sandwiched between gas and water in medium sized pores (Blunt, 2017). In such systems, it is typically assumed that during steady-state flow all three fluid phases are connected in the pore space: gas is continuous in the larger pores, oil in spreading layers, and water in wetting layers. This assumption is embedded in models, including pore network models (Piri & Blunt, 2005a, 2005b) and empirical expressions for relative permeability (Baker, 1988; Stone, 1970),

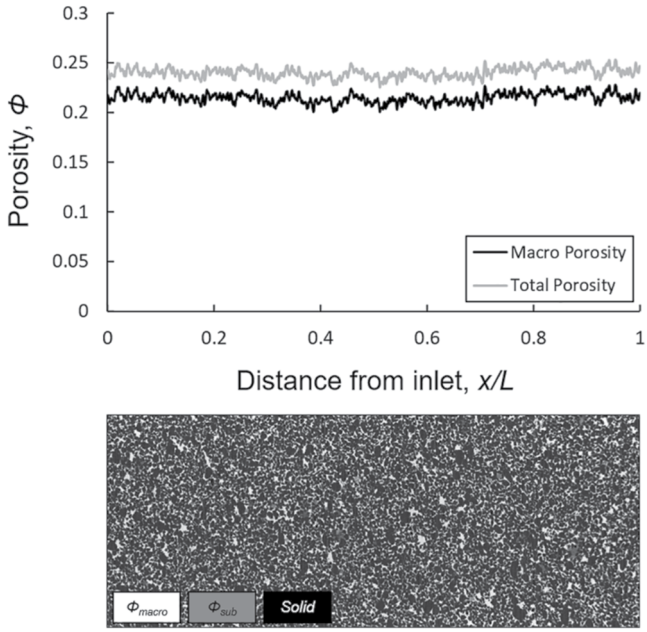

Figure 1. Porosity distribution along the Bentheimer sample characterized using the differential imaging method (Lin et al., 2016). Below is a two-dimensional image of the whole sample, highlighting the macro-pores, sub-resolution pores and the solid rock surface. Solid is shown in black, macro-pores in white, and sub-resolution pores in gray.

that predict three-phase relative permeability. However, in this study, using pore-scale imaging, we show that this assumption is incorrect and in fact, gas flows in disconnected ganglia surrounded by oil and water layers.

Our experiment was conducted under capillary-dominated, immiscible gas-oil conditions. We have designed a new flow cell that enables X-ray imaging at the pore-scale while simultaneously injecting three fluid phases into the rock. Three-phase relative permeability is measured by monitoring the pressure drop across the sample, while saturations are obtained from the high-resolution (5.3 μm/voxel) images. We investigate a saturation history, where the gas fractional flow is first increased and then decreased. We compare our relative permeability measurements with core-scale data, obtained on the same rock type, and show that there is an agreement in the results, indicating the accuracy and applicability of our method. Furthermore, we estimate the capillary pressures by extracting the fluid-fluid interfacial curvatures from the images. In addition, we characterize fluid connectivity, pore occupancy, layer formation and contact angles at different fractional flows.

We show that, contrary to the conventional assumption, gas flows in disconnected ganglia when injected simultaneously with oil and water under steady-state conditions in a water-wet rock. Gas progresses through the center of the pores in the form of discrete blobs surrounded by oil and water layers; it is continuously displaced from the inlet to the outlet by double and multiple displacements. We observe intermittent flow regions, where gas and oil, and water and oil interchangeably occupy the same pores during steady-state flow. This work suggests that in three-phase flow we may never genuinely attain steady-state conditions at the pore-scale, although we have, macroscopically, a constant saturation, since the fluid arrangement at the pore-scale is constantly fluctuating between locations of local capillary equilibrium.

2. Experimental Method

In this section, we first provide details of the rock sample and fluids used to perform the three-phase steady-state experiment. We then move on to describe the newly designed flow cell which permits the simultaneous injection of three fluid phases while allowing for the pressure drop to be recorded and high-resolution pore-scale images to be taken. Next, the set of gas, oil, and water fractional flows selected for the experiment are listed in detail. Finally, we describe the X-ray imaging parameters and image processing techniques implemented to analyze the pore-scale images obtained at different fractional flows.

2.1. Materials

The three-phase steady-state imaging experiment was performed on a Bentheimer sandstone sample of diameter 1.26 cm, and length 4.23 cm. Bentheimer sandstone has a unimodal pore radii distribution, with a mean pore radius of 30 μm, and consists of around 95% quartz with minor amounts of kaolinite and swellable clay minerals (Peksa et al., 2015). The pore size distribution is plotted in Figure S1. The selected sample has a total porosity of 0.24 measured using the differential imaging method (Lin et al., 2016). In this method, the sub-resolution porosity is identified by subtracting a dry image of the sample from one where it is fully saturated with a high-contrast solution. Figure 1 shows the distribution of the image-based porosity across the length of the sample. The absolute permeability (k) of the sample, measured at the experimental conditions, is 1.75 ± 0.03 D ($1.73 \times 10^{-12} \pm 0.03 \times 10^{-12}$ m^2).

In terms of fluids, nitrogen (N_2) was used as the gas phase, n-decane ($C_{10}H_{22}$) as the oil phase, and deionized water (H_2O) as the water phase. To distinguish between the three fluid phases in the X-ray images, 17.5 wt.% Iododecane ($C_{10}H_{21}I$) and 25 wt.% sodium iodide (NaI) were added to the oil and water phases respectively. This process is known as doping, which alters the X-ray attenuation of the fluids providing a different gray-scale value for each phase in the pore-scale images.

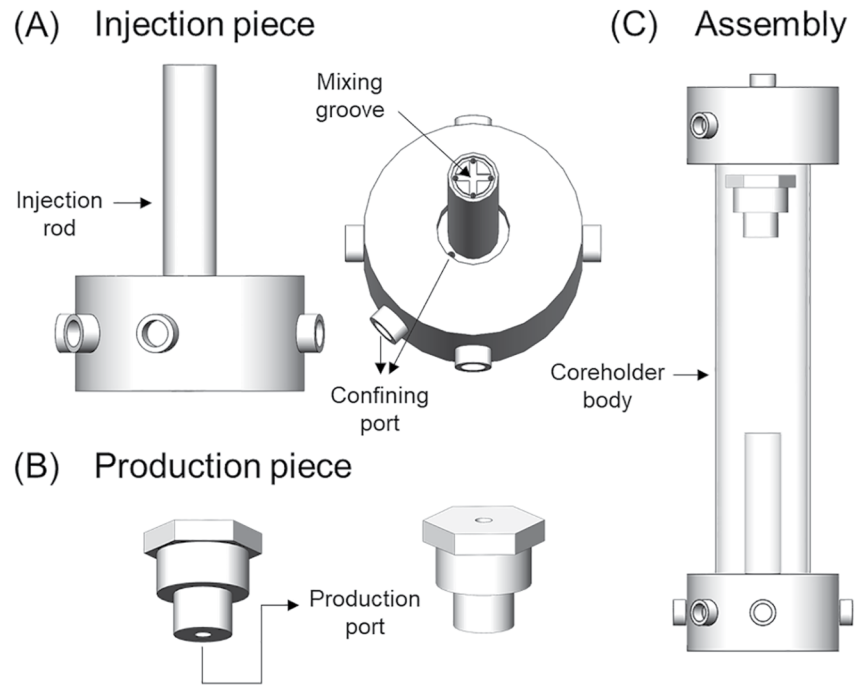

Figure 2. A schematic of the new coreholder design which allows for combining steady-state three-phase relative permeability measurements with pore-scale imaging. The design assembly consists of three main components: (i) injection piece, (ii) production piece, and (iii) coreholder body. Refer to the text for a detailed description of the coreholder design.

The experimental pore pressure was maintained at 1 MPa, and the temperature at 30 °C. At these conditions, gas and oil have dynamic viscosities of $\mu_g = 0.017$ mPa·s (ToolBox, 2018) and $\mu_o = 4.27$ mPa·s (NIST, 2019) respectively, with an interfacial tension of $\sigma_{go} = 11.2$ mN · m^{-1} (Jianhua, 1993). Oil and gas are immiscible at the selected experimental conditions. Water has a dynamic viscosity of $\mu_w = 1.40$ mPa·s with an interfacial tension of $\sigma_{ow} = 52.1$ mN · m^{-1} with oil, and $\sigma_{gw} = 63.7$ mN · m^{-1} with gas (Alhosani, Scanziani, Lin, Selem, et al., 2020; Jianhua, 1993; NIST, 2019).

The spreading coefficients (C_s) with an interfacial tension of $C_{si} = \sigma_{jk} - \sigma_{ij} - \sigma_{ik}$, where i, j, and k denote the three fluid phases. The only positive spreading coefficient is of oil ($C_{so} = +0.4$ mN · m^{-1}), indicating that it is only possible for oil to spread in layers sandwiched between the other two phases in the pore space.

2.2. Steady-State Flow and Imaging Apparatus

To perform a three-phase steady-state flow experiment, three fluid phases must be simultaneously injected into the sample while recording the differential pressure drop across the system. While this can be achieved in the lab, the difficult part in our experiment is integrating this process with pore-scale imaging. Acquiring high-resolution, micro-scale images requires the X-ray source to be placed close to the sample. However, having four injection ports (three ports for fluid injection and one for pressure measurement), would require a large fluid injection piece; therefore, the source must be pushed away from the sample, which reduces the spatial resolution of the images.

To overcome this issue, we designed, in-house, a new coreholder, flow cell, which consists of three primary components: (i) injection piece, (ii) production piece, and (iii) coreholder body, see Figure 2. The injection piece was made of stainless steel and has four injection ports that are in direct contact with the sample inlet. Stainless steel was chosen since it is highly resistant to corrosion and can withstand high operating pressures and temperatures. There is an additional confining port which is used to inject a confining fluid into the coreholder annulus. Figure 2a shows that there is a mixing groove that connects the four injection ports. This groove was placed to allow for the three fluid phases to mix before entering the sample, therefore, preventing the accumulation of the phases on the side of their injection port. The fourth port is needed to measure the pressure at the inlet of the sample. The

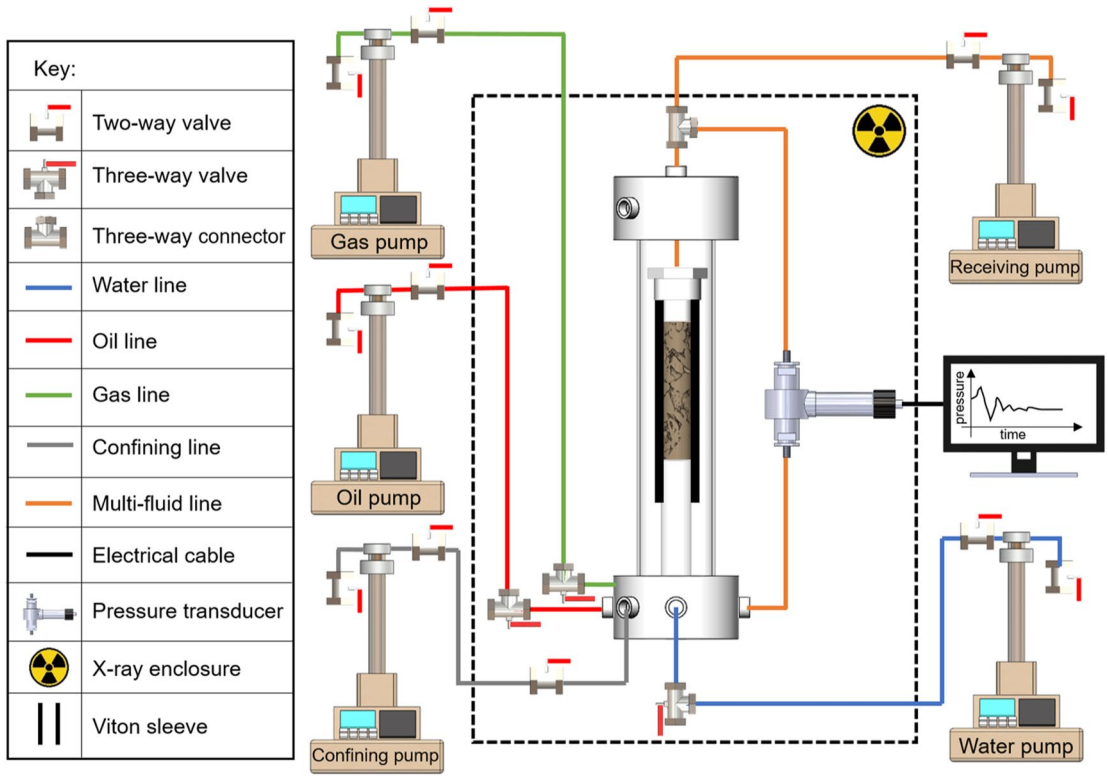

Figure 3. The combined steady-state three-phase flow and pore-scale X-ray imaging apparatus. The dashed line represents the micro-CT enclosure. The coreholder, pumps, flow lines, valves, and pressure transducer in the experiment were assembled as shown in the schematic diagram.

injection rod is around 12 mm in diameter allowing for X-ray images to be acquired at a resolution of 5.3 μm per voxel which is sufficient to capture the pore-scale properties during steady-state three-phase flow.

The production piece has a single port to allow for the displaced fluid phases to be produced (Figure 2b). The outlet pressure is measured downstream of the production piece, outside the coreholder assembly. The coreholder body is made of a thermoplastic polymer known as Polyether ether ketone (PEEK), as opposed to more conventional carbon fiber designs (Andrew et al., 2014a); PEEK is almost X-ray transparent. The PEEK walls are around 3 mm thick which results in a stiff cylindrical design that shows no/little movement as it rotates when mounted with stainless steel end pieces at high pressure and temperature conditions. Minimizing movement during rotation is key to performing repeat X-ray imaging experiments.

The combined pore-scale imaging and steady-state three-phase flow apparatus is shown in Figure 3. The apparatus consisted of five Teledyne Isco pumps, a Keller PD-33X differential pressure transducer, the newly designed PEEK coreholder and a Zeiss Xradia 510 micro-CT scanner.

2.3. Three-Phase Relative Permeability Experiment

The steady-state three-phase relative permeability experiment was performed with constant flow rates at 30°C and 1 MPa pore back pressure. A net confining pressure of 2 MPa was applied at all fractional flows, and the differential pressure was measured with an accuracy of ±0.03 kPa. The fluids were always injected from the bottom of the sample as shown in Figure 3. The impact of gravity on the flow of fluids during the experiment was assessed using the Bond number, shown in the Supporting Information S1. The Bond number indicates that at the pore-scale, the gravitational forces are small compared to the capillary pressure and therefore are insignificant. However, they could have an effect on the macroscopic properties, such as saturation, at the full sample length-scale. Nonetheless, as shown later in Section 3.5, we see almost constant fluid saturations in the experiment and no evidence of a capillary pressure gradient.

Table 1
The Set of Gas, Oil, and Water Fractional Flows at Which Steady-State Conditions Were Reached in the Three-Phase Flow Experiment. f and Q Refer to the Fractional Flow and the Flow Rate, Respectively

Flooding step	f_w	f_o	f_g	Q_w (mL/min)	Q_o (mL/min)	Q_g (mL/min)
1	1	0	0	0.8	0	0
2	0	1	0	0	0.8	0
3	0.5	0.5	0	0.4	0.4	0
4	0.25	0.25	0.5	0.2	0.2	0.4
5	0.125	0.125	0.75	0.1	0.1	0.6
6	0	0	1	0	0	0.8
7	0.125	0.125	0.75	0.1	0.1	0.6
8	0.1875	0.1875	0.625	0.15	0.15	0.5
9	0.25	0.25	0.5	0.2	0.2	0.4
10	0.3125	0.3125	0.375	0.25	0.25	0.3
11	0.375	0.375	0.25	0.3	0.3	0.2

Note. Subscripts w, o and g refer to the water, oil and gas phases respectively. The total flow rate in the experiment was Q_t = 0.8 mL/min. Gas was introduced into the system in flooding step 4, with maximum gas fractional flow $f_g = 1$ reached in step 6.

In this study, three-phase steady-state conditions were reached at various gas, oil, and water fractional flows (f_g, f_o, and f_w) by keeping constant fluid flow rates with a total flow rate of $Q_t = 0.8$ mL/min. The fractional flows selected for the experiment are listed in Table 1. The waiting time for each fractional flow to reach steady-state conditions was at least 12 hr. After that, we waited until the differential pressure was constant over a period of at least 1 hr, to record the pressure drop and start X-ray imaging to determine the fluid saturations.

The experiment was performed under capillary-dominated conditions. The capillary numbers between any two fluid pairs i and j were calculated at different fractional flows using $Ca_{ij} = \mu_i q_i/\sigma_{ij}$, where σ_{ij} is the interfacial tension between the phases, μ_i is the viscosity of the injected fluid and q_i is its Darcy velocity. As a characteristic of water-wet media with spreading oil layers surrounding the gas, we assume that gas and water can only displace oil, while oil can displace both gas and water; gas and water cannot directly displace each other, as we will show later. Table 2 lists the possible displacement capillary numbers at different fractional flows during the experiment. The highest capillary number is 3.15×10^{-6} corresponding to a displacement of gas by oil in flooding step 11, see Table 2, which is still in the capillary-dominated flow regime; see Figure S7.

The selection of the set of fractional flows was done with special care to follow a certain saturation history and avoid any unwanted irreversible switch between drainage and imbibition displacement processes. In this experiment, we investigate the impact of a saturation history, where the gas fractional flow is first increased and then decreased, on three-phase relative permeability. To do so, we adopt an approach in which we keep the oil and water saturation changes in the same direction, while keeping oil and water flow rates the same (treating them as a single phase) – and change the gas saturation in the opposite direction (Alizadeh & Piri, 2014a, 2014b; Oak, 1990; Oak et al., 1990; Saraf et al., 1982). This can be seen in Table 1, where, first, the gas flow rate is increased and oil and water flow rates are decreased in steps 4, 5, and 6, and then gas rate is decreased and oil and water are increased in steps 7, 8, 9, 10, and 11.

The experimental protocol followed to initiate the steady-state three-phase flow micro-CT imaging experiment is described below:

Table 2
The Gas-Oil, Oil-Gas, Oil-Water and Water-Oil Capillary Numbers Calculated at Different Fractional Flows During the Steady-State Three-Phase Flow Experiment

Flooding step	$Ca_{[go]}$	$Ca_{[og]}$	$Ca_{[ow]}$	$Ca_{[wo]}$
1	-	-	-	-
2	-	-	1.81×10^{-6}	-
3	-	-	9.05×10^{-7}	3.39×10^{-7}
4	1.79×10^{-8}	2.10×10^{-6}	4.52×10^{-7}	1.69×10^{-7}
5	2.68×10^{-8}	1.05×10^{-6}	2.26×10^{-7}	8.48×10^{-8}
6	3.57×10^{-8}	-	-	-
7	2.68×10^{-8}	1.05×10^{-6}	2.26×10^{-7}	8.48×10^{-8}
8	2.23×10^{-8}	1.57×10^{-6}	3.39×10^{-7}	1.27×10^{-7}
9	1.78×10^{-8}	2.10×10^{-6}	4.52×10^{-7}	1.69×10^{-7}
10	1.34×10^{-8}	2.63×10^{-6}	5.65×10^{-7}	2.12×10^{-7}
11	8.94×10^{-9}	3.15×10^{-6}	6.78×10^{-7}	2.54×10^{-7}

Note. Capillary numbers were calculated using $Ca_{ij} = \mu_i q_i/\sigma_{ij}$, where σ_{ij} is the interfacial tension between the phases, μ_i is the viscosity of the displacing fluid and q_i is its Darcy velocity. A gas-oil number represents the capillary number calculated when gas displaces oil in the pore space, as is the case for the other pairs. Refer to Table 1 for the fractional flows of each flooding step.

1. First, the sample was wrapped with aluminum foil and inserted in a Viton sleeve. The bottom and top ends of the Viton sleeve were mounted on the injection and production pieces respectively as shown in Figure 3. The Viton sleeve sealed the rock sample from coming into contact with the confining fluid.
2. The coreholder was then placed inside the micro-CT enclosure and all the pumps and flow lines were connected as shown in Figure 3. The differential pressure transducer was connected to the inlet and outlet to measure the pressure drop across the sample.
3. The empty annulus space between the Viton sleeve and the PEEK coreholder body was filled with the confining fluid, deionized water, and a net confining pressure of 2 MPa was applied. At this point a dry scan of the sample was acquired at 5.3 μm/voxel resolution.
4. 200 pore volumes (PV) of water (25 wt.% NaI) were injected into the sample to fully saturate the pore space and the pore pressure was raised to 1 MPa using a back-pressure pump. Water was injected at four flow rates (0.2, 0.4, 0.6 and 0.8 mL/min) while recording the stable pressure drop to calculate the absolute permeability of the sample, which was found to be $1.73 \times 10^{-12} \pm 0.03 \times 10^{-12}$ m^2 ($k = 1.75 \pm 0.03$ D). A 5.3 μm/voxel water saturated scan was acquired at this point, which allowed for the characterization of the porosity distribution, including sub-resolution porosity, of the sample using the differential imaging method (Lin et al., 2016), see Figure 1.
5. Oil (17.5 wt.% $C_{10}H_{21}I$) was injected into the sample at a flow rate of 2 mL/min to reach the irreducible water saturation. The flow rate was then dropped to 0.8 mL/min to measure the pressure drop and a scan was acquired.
6. Water and oil were then simultaneously injected at $f_w = 0.5$, with a total flow rate $Q_t = 0.8$ mL/min, to initiate the sample for the three-phase relative permeability experiment. After reaching steady-state conditions between oil and water, the pressure drop was recorded, and a scan of the sample was acquired.
7. Gas, oil and water were then simultaneously injected into the sample at the fractional flows listed in Table 1. The pressure drop was recorded and scans were taken once steady-state had been reached for each fractional flow to calculate the three-phase relative permeabilities. The gas flow rate was not increased when $f_g = 1$ (flooding step 6, see Table 1).

After the experiment, the rock was taken out and cleaned using DI water to remove any residual gas and oil. The sample was then prepared for a repeat experiment, following the same steps mentioned here. In the repeat experiment, we only investigated one set of fractional flows ($f_g = 0.5, f_{w,o} = 0.25$) during both increasing and decreasing gas flow paths. The repeat experiment was performed to verify if the gas phase was disconnected during steady-state injection, see Section 3.4; therefore, no pressure measurements were recorded.

2.4. X-Ray Image Acquisition and Processing

For every fractional flow, after reaching steady-state conditions, three-dimensional images of the sample and fluids within it were acquired using the ZEISS Xradia 510 Versa micro-CT scanner. The photon energy and power were set to 80 keV and 7 W, respectively at the X-ray source, with a 360° sample rotation angle. Air was the only filter used between the source and sample. A flat panel with a large field of view (12.45 × 12.45 × 10.23 mm) at a resolution of 5.3 μm/voxel was employed at the detector. The exposure time was set to 1.60 s with a total of 3,201 projections. Five images, with a 3.55 mm vertical overlap, were acquired during each scan to capture the length of the whole sample.

The images acquired were then reconstructed, normalized, registered, and stitched to obtain three-dimensional steady-state images of the rock and fluids at each fractional flow, see Figures 4 and 5.

Image segmentation was then performed to obtain quantitative information, including saturations, fluid-fluid curvatures and surface areas. First, to make the segmentation process simpler we decided to ignore the fluid saturations in the sub-resolution porosity; sub-resolution porosity was segmented as a part of the rock phase, except when we characterized the porosity distribution along the sample in Figure 1. This assumption is reasonable, as in water-wet systems, the sub-resolution porosity remains 100% water saturated, hence, it would not have a major impact on the three-phase experimental results.

As mentioned in the Introduction, we see some regions of the pore space with intermediate gray-scale values. We hypothesize that these are places where, during the time of the scan, the pore space was occupied for some time by oil and for some time by gas or water. In theory, therefore, the fluids in the macro-pores should be segmented

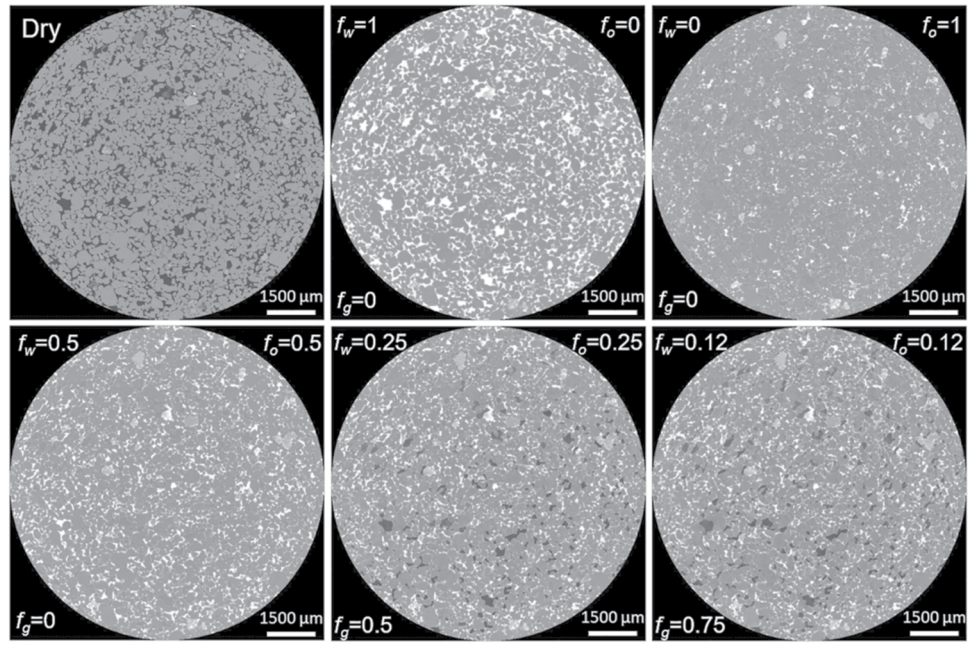

Figure 4. Two-dimensional cross-sectional raw images of the sample acquired during the steady-state three-phase relative permeability experiment. In each image, the gas, oil and water fractional flows (f_g,f_o, and f_w) are stated. The rock, oil, gas, and water are shown in light gray, dark gray, black, and white, respectively.

into seven different phases: (i) water; (ii) oil; (iii) gas; (iv) gas from intermittent gas-oil regions; (v) oil from intermittent gas-oil regions; (vi) oil from intermittent oil-water regions; and (vii) water from intermittent oil-water regions. However, this is impractical, especially with our current image segmentation capabilities. Therefore, to simplify the segmentation process, while minimizing the impact on the quantitative results we decided to do the

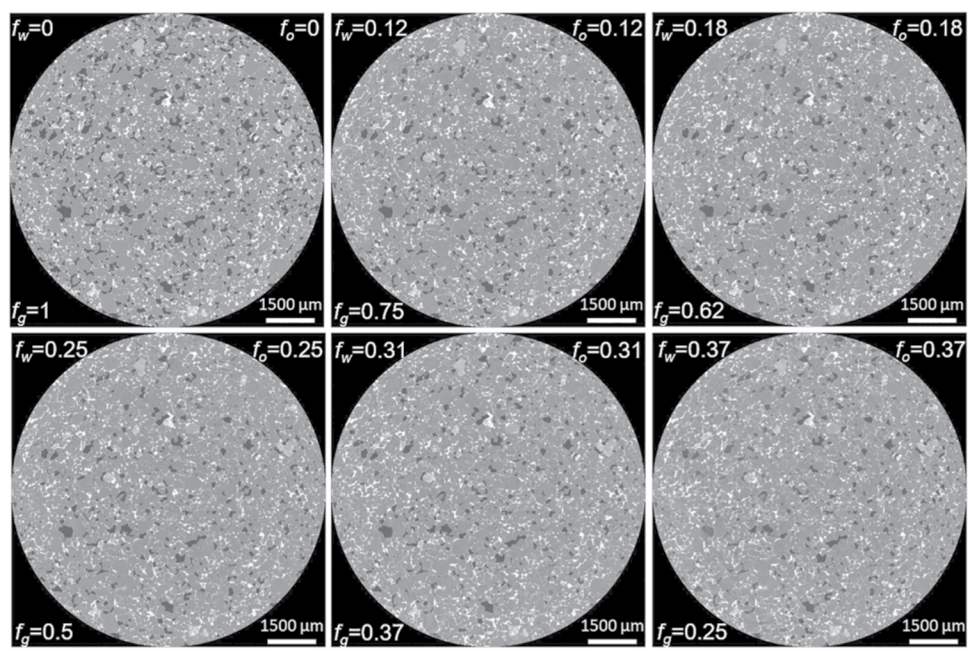

Figure 5. Two-dimensional cross-sectional raw images of the sample acquired during the steady-state three-phase relative permeability experiment. In each image, the gas, oil and water fractional flows (f_g,f_o, and f_w) are stated. The rock, oil, gas, and water are shown in light gray, dark gray, black, and white respectively.

following: (a) ignore the oil-water intermittent flow regions, since oil-water intermittency does not occur very often, that is, ignore phases (vi) and (vii); (b) segment the gas from intermittent gas-oil regions as part of the gas phase, combining phases (iii) and (iv); and (c) segment the oil from intermittent gas-oil regions as part of the oil phase, combining phases (ii) and (v). This leaves us with three phases to segment from the pore-scale images.

To segment the images into these three phases, we used an approach that combines differential imaging with the interactive thresholding segmentation technique. Intermittent regions display a gray-scale value that is in-between the gray-scale values of the two intermittent phases. Therefore, using differential imaging was needed to widen the gray-scale histograms between the intermittent phases, while thresholding was used to assign 50% of the intermittent region to each phase.

The segmentation procedure was as follows: (a) the rock phase was directly segmented from the dry scan, and was used subsequently in all the images; (b) for each fractional flow, the image was subtracted from the high contrast water scan ($f_w = 1$), eliminating the water and rock phases, which leaves the oil and gas phases only in the differential image, with wide gray-scale histograms; (c) the interactive thresholding technique was then used to directly segment the oil and gas phases from the differential images; finally (d) the segmented oil and gas phases were then added to the segmented rock phase in step (a), and the rest of the unassigned voxels were considered as the water phase. The segmentation procedure is explained in more detail in Figure S2.

2.5. Data Analysis

2.5.1. Relative Permeability

The three-phase relative permeabilities were calculated using the multiphase flow Darcy equation (Blunt, 2017):

$$k_{rg} = \frac{q_g \mu_g L}{\Delta P k} \tag{1}$$

$$k_{ro} = \frac{q_o \mu_o L}{\Delta P k} \tag{2}$$

$$k_{rw} = \frac{q_w \mu_w L}{\Delta P k} \tag{3}$$

where k_r is the relative permeability, q is the Darcy velocity (flow rate per unit area), μ is the viscosity, k is the absolute permeability, ΔP is the pressure drop, and L is the sample length. Subscripts g, o, and w refer to the gas, water and oil phases, respectively.

While the pressure drop was measured using the differential pressure transducer, the fluid saturations at each fractional flow were measured on the segmented pore-scale images. Only fluid saturations in the macro-pore space were considered, see Section 2.4 for more details.

2.5.2. Capillary Pressure

Pore-scale imaging allows us to capture the interface between the fluid phases from segmented images. By measuring the curvature of the interface between any fluid pair, oil-water, gas-oil, and gas-water, we can simply find their local capillary pressure. This is made possible using the Young-Laplace equation which directly relates the capillary pressure P_{cij} to the interfacial curvature κ_{ij} through interfacial tension σ_{ij} (Armstrong et al., 2012):

$$P_{c,ij} = \sigma_{ij} \kappa_{ij} \tag{4}$$

for any combination of phases i and j.

We used a method previously established in the literature to characterize the interfacial curvature from pore-scale images (Akai et al., 2019; Armstrong et al., 2012). First, the interface between the fluid pairs was extracted from the segmented images and smoothed with a kernel size of 5, in the direction of the less wetting phase, gas in the case of gas and oil and gas and water, and oil in the case of oil and water, to remove any voxelization artifacts. The total curvatures were then measured on the smoothed interfaces by fitting them with a quadratic surface.

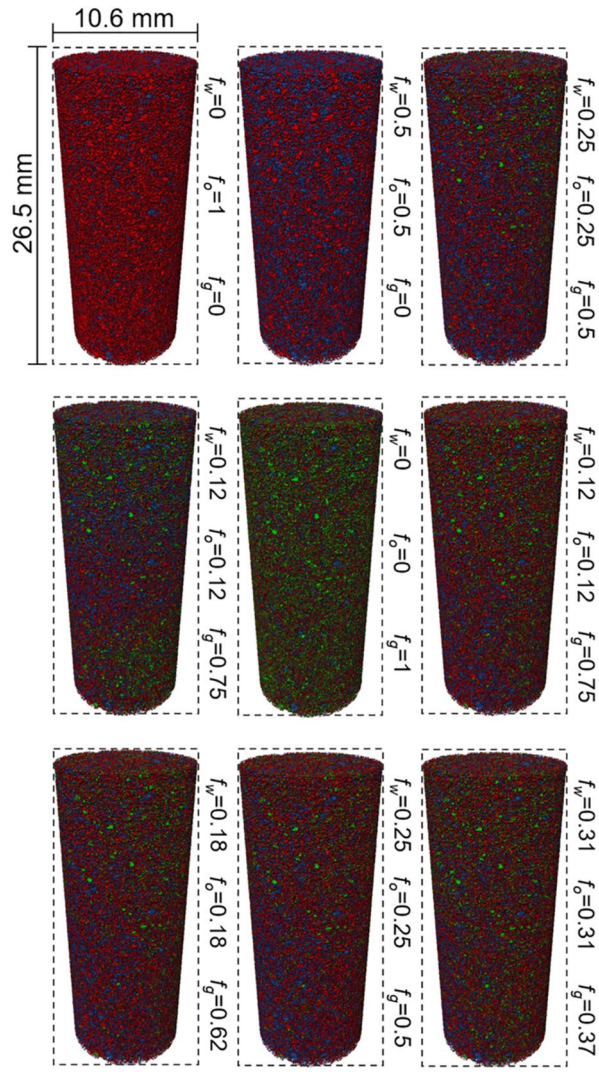

Figure 6. Three-dimensional volume rendering of the fluid configurations in the pore space during the three-phase steady-state experiment at different fractional flows. Gas is shown in green, water in blue and oil in red. The rock is rendered transparent. Gas, oil, and water fractional flows (f_g,f_o, and f_w) are stated.

3. Results and Discussion

Here, we present the pore-scale findings obtained, using X-ray imaging, from the steady-state three-phase flow experiment. First, in Section 3.1, we present measurements of the fluid-fluid contact angles to confirm the water-wet state of the rock, followed by a characterization of the pore occupancy in Section 3.2. Then, in Section 3.3, we display measurements of the fluid-fluid and fluid-solid specific interfacial areas. These results, alongside the fluid connectivity in Section 3.4, are used to explain the three-phase relative permeability behavior in Section 3.5. Evidence of intermittent flow regions is presented in Section 3.6. The measured local capillary pressures between the three fluid pairs are shown in Section 3.7. Finally, in Section 3.8, three-dimensional images illustrating the occurrence of double displacement processes are presented.

Figure 6 shows the constructed three-dimensional images of the fluid configurations in the pore space at different fractional flows.

3.1. In Situ Wettability Characterization

The oil-water, gas-oil, and gas-water contact angles were characterized on the same segmented subvolume, of size 2.65 × 2.65 × 2.65 mm, at different fractional flows using an automated algorithm that measures the geometric angle on the three-phase contact line between each fluid pair (AlRatrout et al., 2017). Wettability is typically determined using the oil-water contact angle; an angle lower than 90° is indicative of a water-wet system, while oil-wet conditions have angles larger than 90° (Blunt, 2017; Salathiel, 1973).

The geometric oil-water contact angles, measured through the denser phase (water), are shown in Figure 7. The mean oil-water contact angle, for all fractional flows, is 61° ± 16°, confirming the water-wet nature of the sample. This is also evident from the two-phase pore-scale images shown in Figure 7 (right), where oil resides in the center of the pores surrounded by water wetting layers. Furthermore, Figure 7 (left) illustrates that there was no wettability alteration throughout the flooding experiment; the contact angle between oil and water remains approximately constant. This also indicates that the geometric oil-water contact angle is independent of saturation history; the oil-water angle was not impacted by switching the saturation path.

As expected, due to the positive initial oil spreading coefficient (C_{so} = +0.4 mN · m^{-1}), see Section 2.1, oil spreads in layers surrounding the gas phase which results in an effective gas-oil contact angle of zero; oil is strongly wetting to gas. This is evident from Figure 8, where the three-dimensional arrangement of gas, oil and water in a single pore is presented; gas is shown in green, oil in red, water in blue, while the rock phase is rendered semi-transparent (gray). As soon as gas contacts oil, oil spreads in layers sandwiched between gas and water in the pore space. The presence of oil in layers prevents gas from directly contacting water in the pore space; therefore, we were unable to measure the geometric contact angle between gas and water. The measured contact angles are consistent with measurements previously made on water-wet rocks at immiscible gas-oil conditions (Andrew et al., 2014a, 2014b; Scanziani, Singh, et al., 2018).

3.2. Pore Occupancy

The size of the pores occupied by the three fluid phases, also known as pore occupancy, was determined using an approach developed by Scanziani, Singh, et al. (2018) which combines the maximal ball method with the generalized network extraction algorithm (Bultreys et al., 2015; Dong & Blunt, 2009; Raeini et al., 2017). The pore network model is first extracted from a dry scan of the rock, where the pores are represented by spheres and their

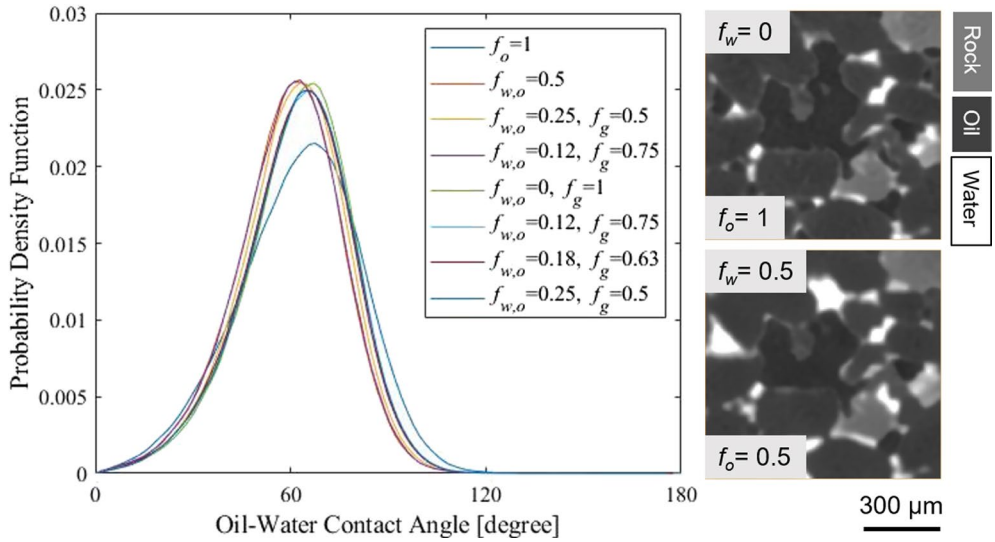

Figure 7. (left) Probability density function of the in situ measured oil-water contact angles throughout the steady-state three-phase flow experiment at different fractional flows. (right) Two-dimensional pore-scale images of the same pore, at two different fractional flows, illustrating that oil resides in the centers in the presence of water, confirming the water-wet state of the rock sample. The contact angles were measured through the denser phase using an automated algorithm developed by AlRatrout et al. (2017). f_w and f_o refer to water and oil fractional flows respectively.

size is the diameter of the sphere. The spheres are then imposed on the pore-scale images acquired at different fractional flows, and each sphere is assigned to a phase depending on the gray-scale value that lies in its center: we do not consider intermittency and assign a unique occupancy dependent on the average gray-scale level. Pore occupancy was characterized on images, of size 7.95 × 7.95 × 15.9 mm, located in the center of the sample, for all fractional flows, where gas fractional flow (f_g) is first increased while oil and water (f_o and f_w) are decreased, and then gas is decreased while oil and water are increased, see Figure 9.

Figure 9a shows that when oil is first injected into the water-wet rock, it invades the largest pores confining water to smaller ones, as expected (Scanziani, Singh, et al., 2018). During the subsequent injection of oil and water, water imbibes into the corners in wetting layers, displacing oil in the smaller pores and restricting it to flow in the larger pores. Some oil gets trapped in the center of the pores surrounded by water wetting layers, see Figure 8a.

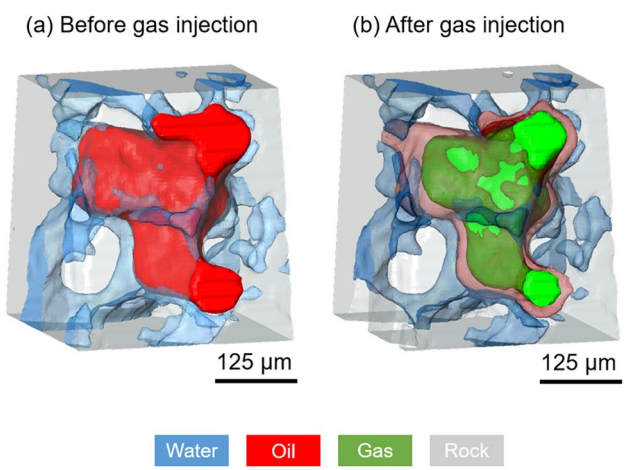

Figure 8. Three-dimensional representation of the fluids arrangement in a single pore (a) before gas injection, and (b) after gas injection. Oil is shown in red, water in blue, gas in green, while the rock is rendered semi-transparent (gray).

During the simultaneous injection of gas, oil and water, gas replaces oil in the larger pores, forcing it to flow in spreading layers in the medium sized pores, while water flow is restricted to smaller pores, see Figure 9c. Some of the oil that was trapped during two-phase flow gets reconnected in regions of the pore space smaller than those occupied before as a consequence of oil spreading. As the gas fractional flow is increased, the oil and water flows decrease, Figures 9d and 9e, gas squeezes more oil and water into smaller sized pores. From this we can establish a clear wettability order in the system, where water is the most-wetting phase, residing in the smallest pores, gas is the most non-wetting phase, occupying the biggest pores, while oil, is the intermediate-wet phase, spreading in layers sandwiched between gas and water, and filling medium sized pores; this wettability order is also evident from Figure 8b. This is consistent with previous experiments conducted on water-wet media at immiscible gas-oil conditions (Feali et al., 2012; Øren et al., 1992; Scanziani, Singh, et al., 2018).

However, we observe a unique pore occupancy behavior as the saturation path is reversed, that is, the gas fractional flow is decreased, while the oil and water fractional flows are increased. There is little/no change in the three-phase pore occupancy when f_g is decreased, as opposed to increasing

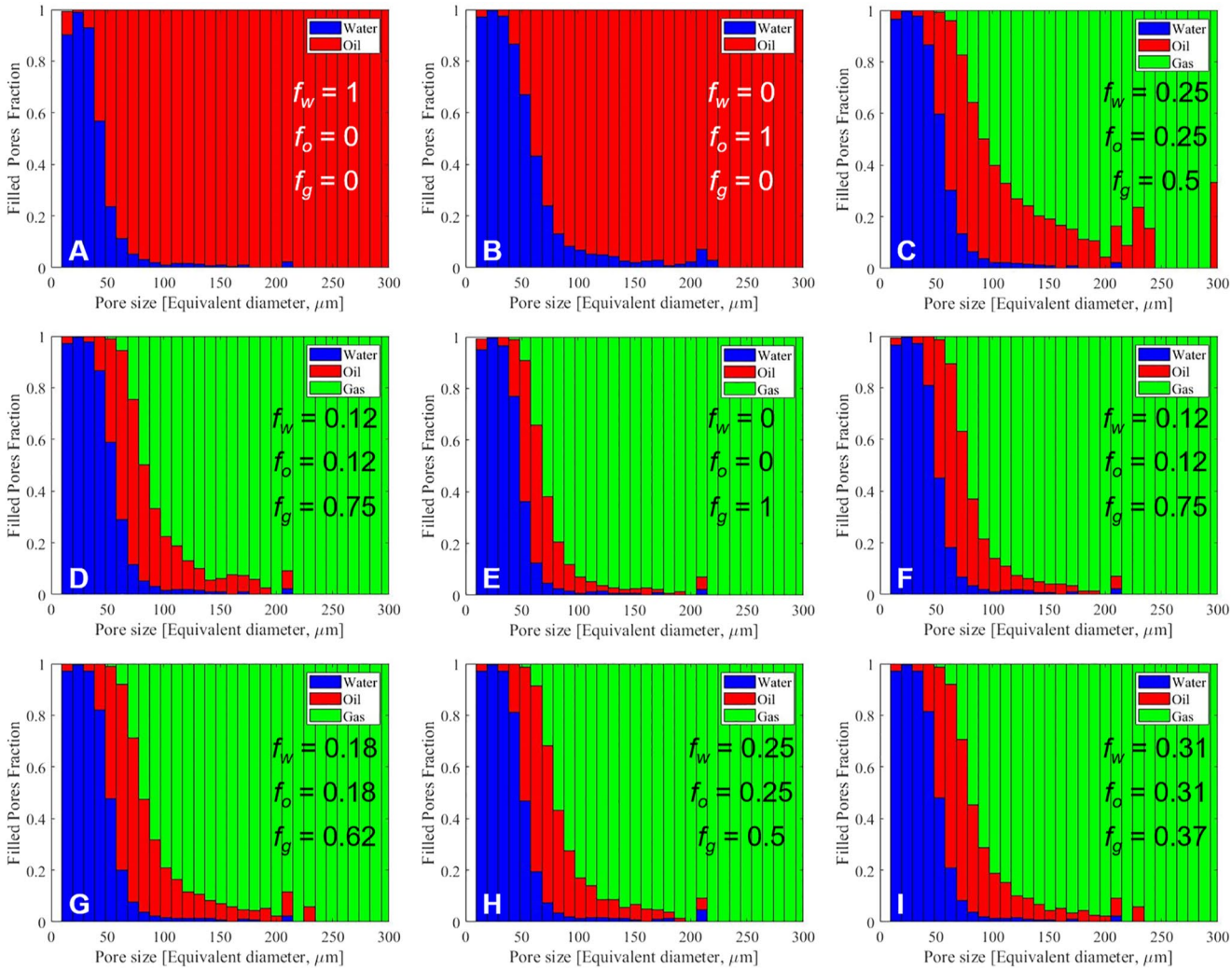

Figure 9. Stacked bar charts showing the pore occupancy in the pore space of the rock at different fractional flows. The phase that occupies the center of the pore is considered to occupy the pore. The size of the pores is determined by fitting them with inscribed spheres, the diameter of the sphere is the diameter of the pore. Pore occupancy was quantified on images of size 7.95 × 7.95 × 15.9 mm. Water is shown in blue, oil in red, and gas in green. Gas, oil, and water fractional flows (f_g, f_o, and f_w) are stated in the respective images.

f_g, which implies that pore occupancy is a function of saturation history, see Figures 9f–9h and 9i. This behavior can be ascribed to double capillary trapping, gas trapping by oil and oil trapping by water, which can permanently trap gas in the pore centers. Therefore, regardless of the increase in oil and water fractional flows, they would not be able to displace the trapped gas phase; gas remains trapped in the same pores. Also, since oil and water are injected at the same flow rate, they maintain their previously established pore occupancy. However, this can only be confirmed by looking at the fluid connectivity and saturations as we will show in Sections 3.4 and 3.5. Furthermore, this can have an impact on the relative permeability of oil and water, as having a trapped gas phase can restrict its flow in the pore space.

3.3. Interfacial Areas

Figure 10 shows measurements of the specific interfacial areas, area per unit volume, between the fluids and the fluids and solid quantified on segmented images of the whole sample at different fractional flows: intermittency is not accounted for, instead a single phase label was assigned to all voxels based on their gray-scale values. This meant that an intermittent voxel was either assigned to be gas or oil dependent on the nearest gray-scale value.

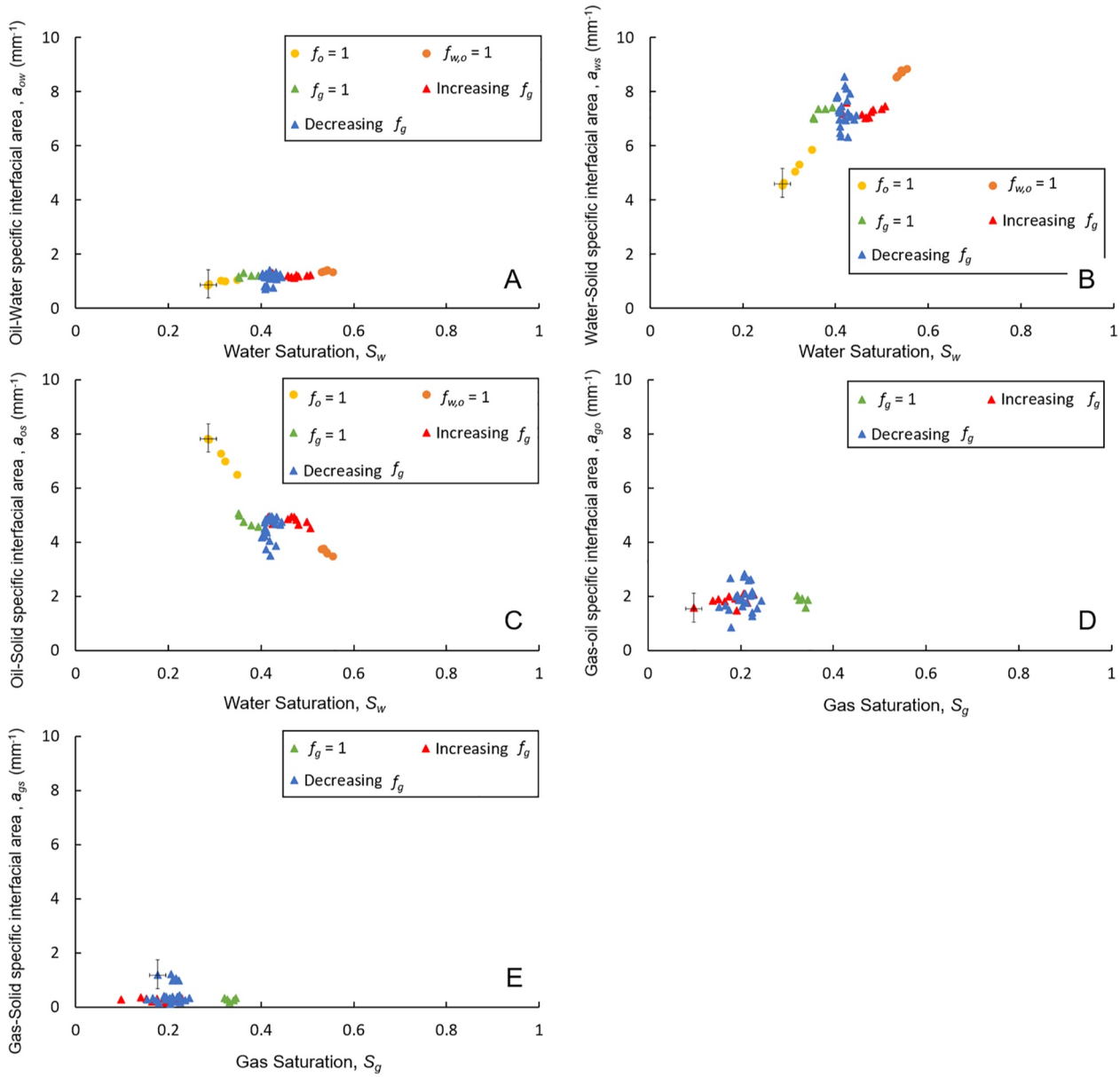

Figure 10. Specific interfacial areas between (a) oil and water, (b) water and solid, (c) oil and solid, (d) gas and oil, and (d) gas and solid measured on segmented images of the whole sample throughout the flooding experiment. Error bars represent uncertainty in the measurements.

The oil-water specific interfacial area remains constant throughout the two- and three-phase steady-state displacements, with values around 1 mm^{-1}, see Figure 10a. The specific interfacial area between oil and water is independent of saturation history under three-phase flow conditions, since the area is dominated by the contact between water in wetting layers close to the solid surface and oil either occupying medium-sized pores, or as a spreading layer surrounding gas. The gas-oil specific area, Figure 10d, is slightly higher than the oil-water one, which can be ascribed to oil being more wetting to gas, than water is wetting to oil; this is reflected in the gas-oil and oil-water contact angles, where $\theta_{go} = 0°$ compared to weakly wetting $\theta_{ow} = 61° \pm 16°$ (Section 3.1) as well as the lower gas-solid area compared to oil-solid. In contrast to the oil-water specific area, the gas-oil area appears to be a function of the saturation history; the gas-oil area remains roughly constant as the gas fractional flow is increased but shows a considerable change when it is decreased, even though the gas saturation is almost the same: as discussed below, this could be a result of intermittency. The gas-water interfacial area is zero since

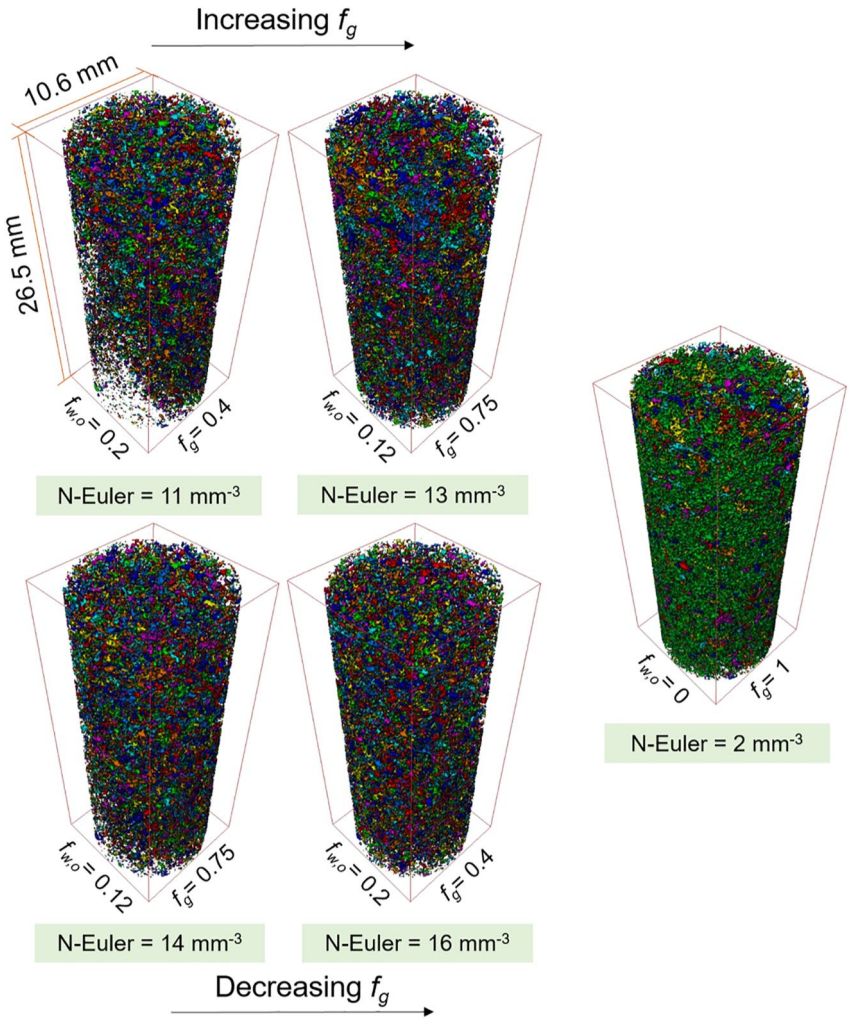

Figure 11. Three-dimensional maps of the in situ gas connectivity in the pore space of the water-wet rock under three-phase steady-state conditions at different gas, oil, and water fractional flows. Each disconnected cluster is labeled with a different color. Gas, oil and water fractional flows (f_g and $f_{w,o}$) are stated. N-Euler refers to the normalized Euler number listed in Table 3. Images on top are acquired during the increasing gas fractional flow path, decreasing oil and water, while on the bottom are images acquired during decreasing gas fractional flow, increasing oil and water. On the right, is the image acquired at a gas fractional flow of 1 which is the only time the gas is connected across the sample.

spreading oil layers prevent direct gas-water contact in the pore space. Oil spreading around gas also reduces the gas-solid specific area, see Figure 10e.

Similar to the gas-oil specific area, the water-solid and oil-solid areas are impacted by the saturation history under three-phase conditions, see Figures 10b and 10c. The huge variability in the gas-oil, gas-solid, and water-solid areas observed around the same saturation, when the gas fractional flow is decreased and oil and water fractional flows are increased can imply that the fluid configurations are constantly fluctuating between locations of local capillary equilibrium, despite having, macroscopically, constant saturations. This phenomenon is discussed in more detail in Section 3.6. Water-solid and oil-solid areas are the highest in the pore space, with a slightly larger water-solid area due to water residing in wetting layers close to the solid surface.

3.4. Fluid Connectivity

Here, we assess the fluid connectivity in the pore space both qualitatively and quantitatively in Figures 11 and 12, and Table 3. To qualitatively examine the connectivity, the fluids were first isolated from the segmented images, and each disconnected object, in the image of the isolated phase, is labeled with a distinct color. Again, all voxels

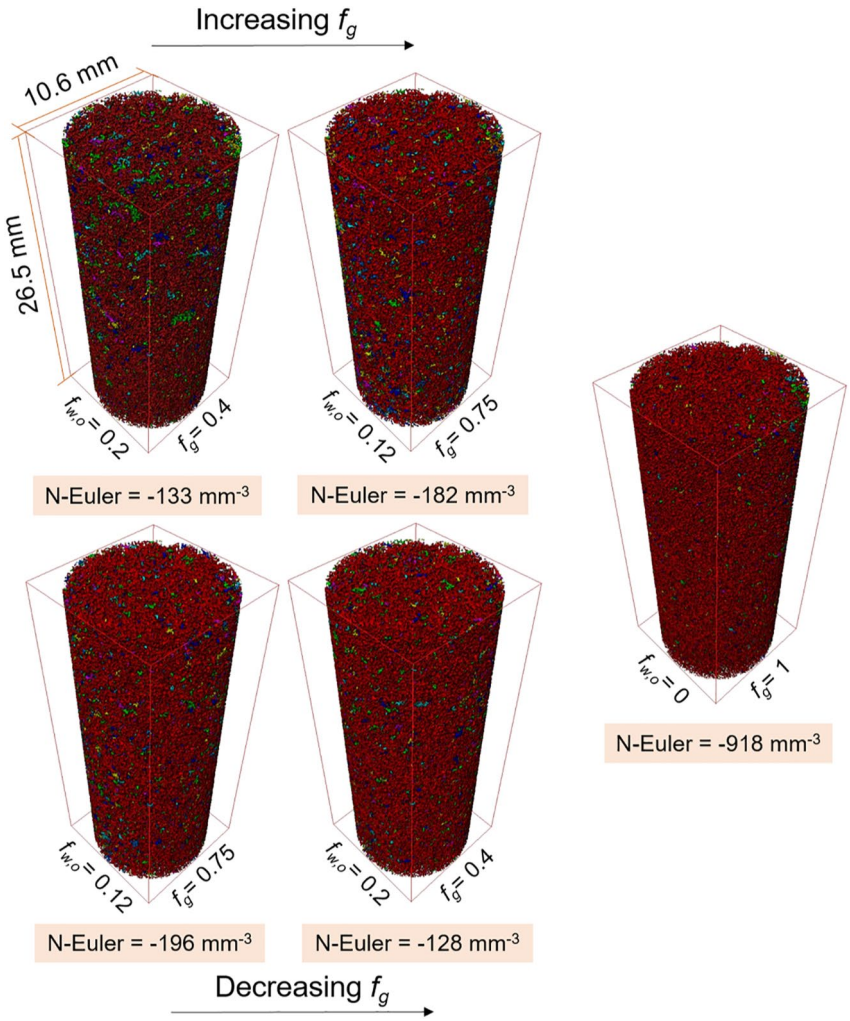

Figure 12. Three-dimensional maps of the in situ oil connectivity in the pore space of the water-wet rock under three-phase steady-state conditions at different gas, oil, and water fractional flows. Each disconnected cluster is labeled with a different color. Gas, oil and water fractional flows (f_g and $f_{w,o}$) are stated. N-Euler refers to the normalized Euler number listed in Table 3. Images on top are acquired during the increasing gas fractional flow path, decreasing oil and water, while on the bottom are images acquired during decreasing gas fractional flow, increasing oil and water. On the right, is the image acquired at a gas fractional flow of 1.

were given a unique phase label: intermittent regions were assigned to either gas or oil phases dependent on the nearest gray-scale value. Figures 11 and 12 show in three-dimensions the in situ connectivity of the gas and oil phases respectively at different fractional flows, a large color range represents a poorly connected phase, while a narrow color distribution indicates better connectivity.

We observe a distinct gas flow pattern during the steady-state flow of gas, oil, and water in the water-wet rock, see Figure 11. Gas, the most non-wetting phase, advances through the pore space in the form of disconnected ganglia; gas is not connected although it is continuously injected into the sample. This gas flow pattern contradicts the conventional assumption that the gas phase is connected in the larger pores in water-wet rocks at steady-state conditions, which is implemented in current three-phase flow models. Instead, by combining pore-scale imaging with steady-state three-phase flow, it has been discovered that gas, in fact, flows in disconnected clusters when injected simultaneously with oil and water in a water-wet system. Disconnected unsteady-state gas flow has been previously observed in a strongly oil-wet three-phase system, where gas was intermediate-wet, using synchrotron X-ray source (Alhosani, Scanziani, Lin, Selem, et al., 2020), but not over a range of fractional flows in steady-state in a water-wet system.

Table 3
Euler Characteristic of Water, Oil, and Gas During the Steady-State Three-Phase Experiment at Different Fractional Flows

				Normalized Euler characteristic [mm^{-3}]		
Flooding step	f_w	f_o	f_g	Water	Oil	Gas
1	1	0	0	-	-	-
2	0	1	0	−4909	1	-
3	0.5	0.5	0	−3781	23	-
4	0.25	0.25	0.5	−3348	−133	11
5	0.125	0.125	0.75	−3149	−182	13
6	0	0	1	−3133	−918	1
7	0.125	0.125	0.75	−3491	−232	15
8	0.1875	0.1875	0.625	−3483	−196	14
9	0.25	0.25	0.5	−3476	−183	16
10	0.3125	0.3125	0.375	−3508	−128	16
11	0.375	0.375	0.25	−3542	−163	18

Note. The Euler number was measured on segmented images of the whole sample and normalized to the total volume. *f* refers to the fractional flow, while subscripts *w*, *o*, and *g* refer to the water, oil, and gas phases respectively.

Furthermore, we see that disconnected gas flow persists under both increasing gas fractional (f_g), decreasing oil and water fractional flows (f_o and f_w), and decreasing f_g (increasing f_o and f_w). This demonstrates that gas never connects across the sample, unless $f_g = 1$, when only gas is flowing, see Figure 11. Therefore, we attribute the flow of gas in disconnected clusters when injected simultaneously with oil and water to the swelling of oil and water in the throats, the restrictions between the pores, continuously trapping gas in the pore centers. Since water and oil invade the pore space in an imbibition process, in the presence of gas, their layers thicken and coalesce in the throats disconnecting the gas phase. Gas is considered trapped in a double capillary trapping mechanism. Therefore, the only way for gas to progress through the pore space is through double and multiple displacement processes, as we will show in Section 3.8. The disconnected flow pattern can have huge implications on the gas relative permeability as we will show in the next section. Moreover, it shows that subsequent water injection, after gas injection, to trap gas is unnecessary in gas storage applications as gas naturally gets disconnected in the pore space (Blunt, 2017). However, intermittent pathways are not included in this analysis which, in theory, can improve the gas connectivity in the pore space.

As mentioned in Section 2.3, we repeated the experiment in the same sample at one set of fractional flows ($f_g = 0.5, f_{w,o} = 0.25$) during both increasing and decreasing gas flow paths to confirm this observation of disconnected gas flow at steady-state conditions. The connectivity results in the repeat experiment are shown in Figure S3. We find that in the repeat experiment gas was also disconnected with positive Euler numbers per unit volume of 31 mm^{-3} and 25 mm^{-3} during increasing and decreasing gas flow paths respectively. These values are even larger than the Euler numbers measured in the main experiment at the same fractional flows in the two flow paths, 11 mm^{-3} and 16 mm^{-3}, respectively, and reinforce the main conclusion that the gas phase is disconnected.

Figure 12 shows the three-dimensional connectivity of the oil at different fractional flows. Here we observe a unique trend in the oil connectivity: oil becomes more connected with increasing gas fractional flow, despite the simultaneous decrease in the oil flow; oil connectivity is enhanced as oil saturation decreases and gas saturation increases. The reason for this behavior is the spreading of oil in connected layers in the presence of gas. As the gas saturation increases, it invades new pores, where oil could be previously trapped by water; the trapped oil is then connected to the spreading oil layer surrounding the invading gas phase. This explanation is supported by examining the oil connectivity at $f_g = 1$, where the gas saturation is the highest, when oil is most connected, see Figure 12. Conversely, oil becomes less connected as the gas fractional flow is decreased, and oil and water fractional flows are increased with trapping of gas. This indicates that, unlike gas, oil connectivity is a function of saturation history.

Furthermore, we quantify the Euler characteristic of oil, water and gas on images of the whole sample to quantitatively assess their connectivity in the pore space at different fractional flows (Herring et al., 2013, 2015; Mecke & Wagner, 1991; Vogel, 2002; Vogel & Kretzschmar, 1996), see Table 3. The Euler number (characteristic) is the number of objects (ganglia) minus the number of redundant loops in the ganglia. We quote values per unit volume. If a phase has a large positive Euler characteristic that means it is trapped into many discrete ganglia, while a large negative Euler characteristic implies a phase that is interconnected with many loops (Herring et al., 2019). Prior to measuring the Euler characteristic, features smaller than 10 voxels in size were filtered out of the images (Alhosani, Lin, et al., 2021; Herring et al., 2019).

The Euler characteristic results in Table 3 confirm that under steady-state three-phase flow conditions, oil and water are connected in spreading and wetting layers respectively, while gas is disconnected in the pore space. Oil connectivity is better under three-phase flow conditions compared to two-phase flow. Again, we see that oil gets more connected as f_g is increased, and less connected as f_g is decreased with maximum connectivity when gas is injected alone ($f_g = 1$). The quantitative results support the qualitative observations that gas is disconnected when injected simultaneously with oil and water, and best connected when injected alone ($f_g = 1$). Water is largely connected in the pore space under both two and three-phase flow conditions, due to its existence in wetting layers.

3.5. Three-Phase Relative Permeability

The gas, oil, and water steady-state relative permeabilities were calculated using the multiphase Darcy equations, Equations (1)–(3). The relative permeability of each phase is plotted as a function of its own saturation. As mentioned in Section 2.4, only the fluid saturations in the macro-pores were considered in this study. The saturation profiles of the three fluid phases, at different fractional flows, are plotted in Figure 13. Notice that Figure 13 is divided into two columns, in the left column, are the saturation profiles for the increasing f_g, and decreasing f_o and f_w, flow path, while on the right are the saturation profiles for the decreasing f_g, and increasing f_o and f_w. The saturation profiles for $f_g = 1$ are plotted in both for reference. The averaged saturations, for all fractional flows, are plotted in a ternary diagram in Figure S4.

Figure 13a shows that the irreducible water saturation reached during two-phase flow, when $f_o = 1$, is around 0.32. The high irreducible water saturation is attributed to the water-wet nature of the rock and the low capillary pressure imposed at the end of primary drainage. Initial oil and water saturations at $f_{w,o} = 0.5$, before gas injection, were 0.46 and 0.54 respectively, see Figures 13a and 13b.

At the first three-phase fractional flow, the gas saturation reached 0.15, with oil and water saturations of 0.38 and 0.47 respectively, see Figures 13a–13c. At the end of the increasing gas saturation flow path, $f_g = 1$, the gas saturation only reached 0.33, with 0.31 and 0.36 oil and water saturations. The water saturation is the highest as it remains connected in wetting layers in the corners of the pore space. Moreover, the gas rate was not increased at $f_g = 1$ which explains the low gas saturation, high remaining oil and water saturations, when gas is injected alone: once gas established a flow path through the sample there was no further displacement. During increasing f_g, and decreasing f_o and f_w, flow path, the gas saturation increased, while the oil and water saturations decreased as expected.

However, in contrast, during the subsequent saturation path, decreasing f_g and increasing f_o and f_w, the fluid saturations remained largely constant regardless of the change in the fluid flow rates, see Figures 13d–13f. This explains why the pore occupancy also remained constant in this saturation path (Section 3.2). As discussed previously, this is due to gas trapping by oil and water layers. As gas gets trapped, it is immobilized in the pore space keeping the gas saturation constant, and since oil and water are injected at the same flow rate their saturations also remain constant. The high residual gas saturation observed indicates that water-wet oil reservoirs are ideal for gas storage applications; the stored gas is permanently immobilized once injection stops.

Nevertheless, since gas is continuously injected, although at lower flow rates than that reached at $f_g = 1$, then some of the apparently trapped gas is displaced by double and multiple displacements. Therefore, we suspect that there are two types of trapped gas ganglia during the decreasing f_g and increasing f_o and f_w flow path: (a) trapped gas which can move at a given flow rate during decreasing f_g and increasing f_o and f_w; and (b) trapped gas which is immobilized permanently unless gas is injected at a higher flow rate than that applied at $f_g = 1$ (higher than 0.8 mL/min). This indicates that fluid saturations are indeed a function of saturation history. The saturation profiles did not show any signs of capillary gradients, the capillary end-effect.

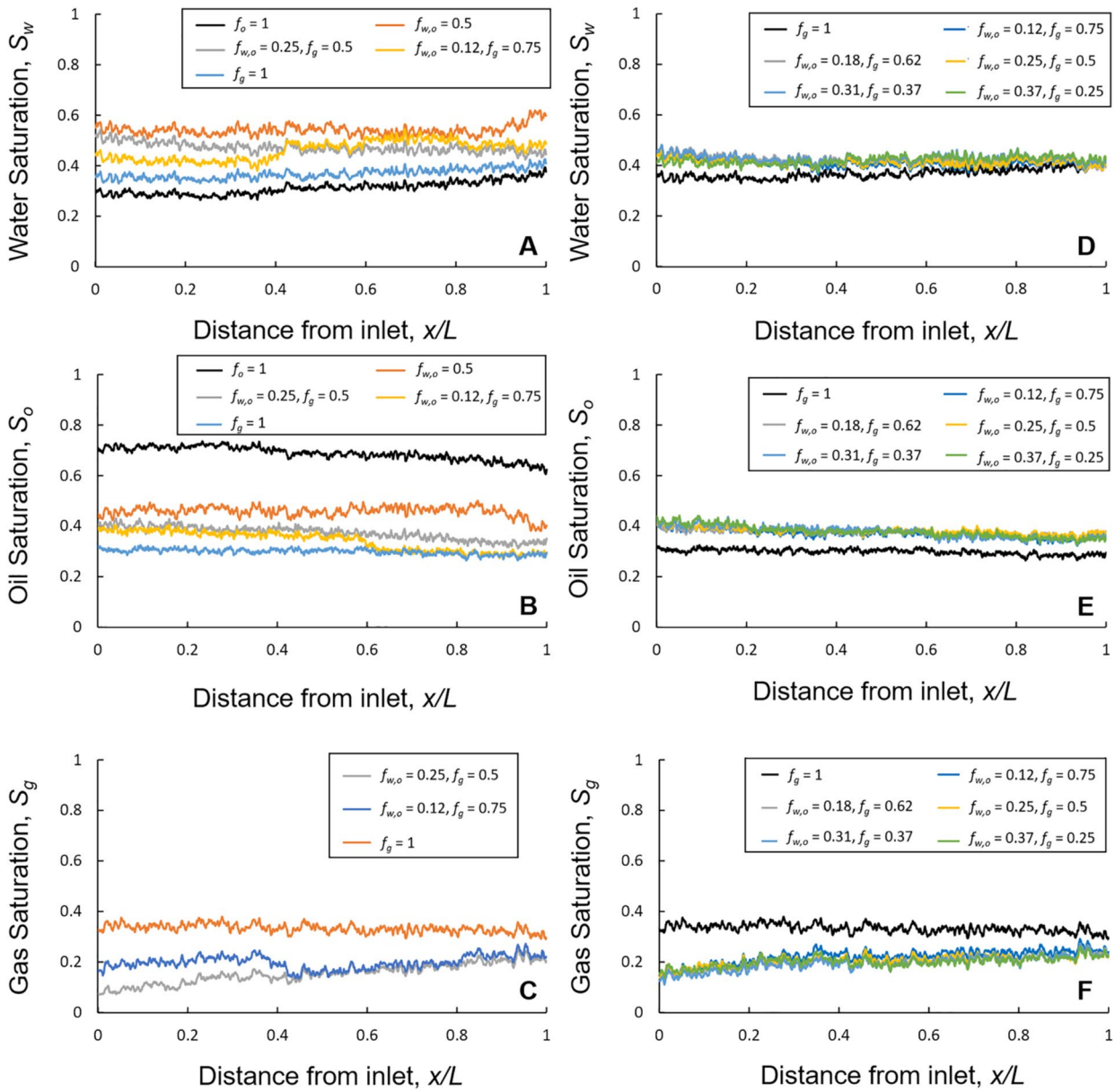

Figure 13. Fluid saturation profiles of (a) water, (b) oil, and (c) gas during increasing gas fractional flow, decreasing oil and water fractional flows, and of (d) water, (e) oil, and (f) gas during decreasing gas fractional flow, increasing oil and water, plotted along the length of the whole sample. Fluid saturations in the macro-pores only are considered. Note that the saturation profiles are approximately constant with distance indicating that there is no noticeable capillary end effect. Gas, oil, and water fractional flows (f_g and $f_{w,o}$) are stated.

Moreover, since we observe, macroscopically, constant fluid saturations but changing fluid-fluid and fluid-solid interfacial areas during decreasing f_g and increasing f_o and f_w, see Figure 10, we hypothesize that during this saturation path we never genuinely attain steady-state conditions at the pore-scale, and that the fluid arrangement is constantly fluctuating between two or more locations of local capillary equilibrium. There is a small gradient in gas saturation with a slight tendency for gas to accumulate near the outlet, the top of the sample, due to the effects of gravitational forces; see the discussion in the Supporting Information S1.

To calculate the three-phase relative permeability, the pressure drop across the sample was measured. The measured differential pressures (ΔP), at all fractional flows are plotted in Figure 14. The reported pressure is the stable differential pressure, at apparent steady-state conditions, measured over a period of 1 hr, after a minimum waiting time of at least 12 hr for each fractional flow. Reported in Figure 14 are the mean pressure values used

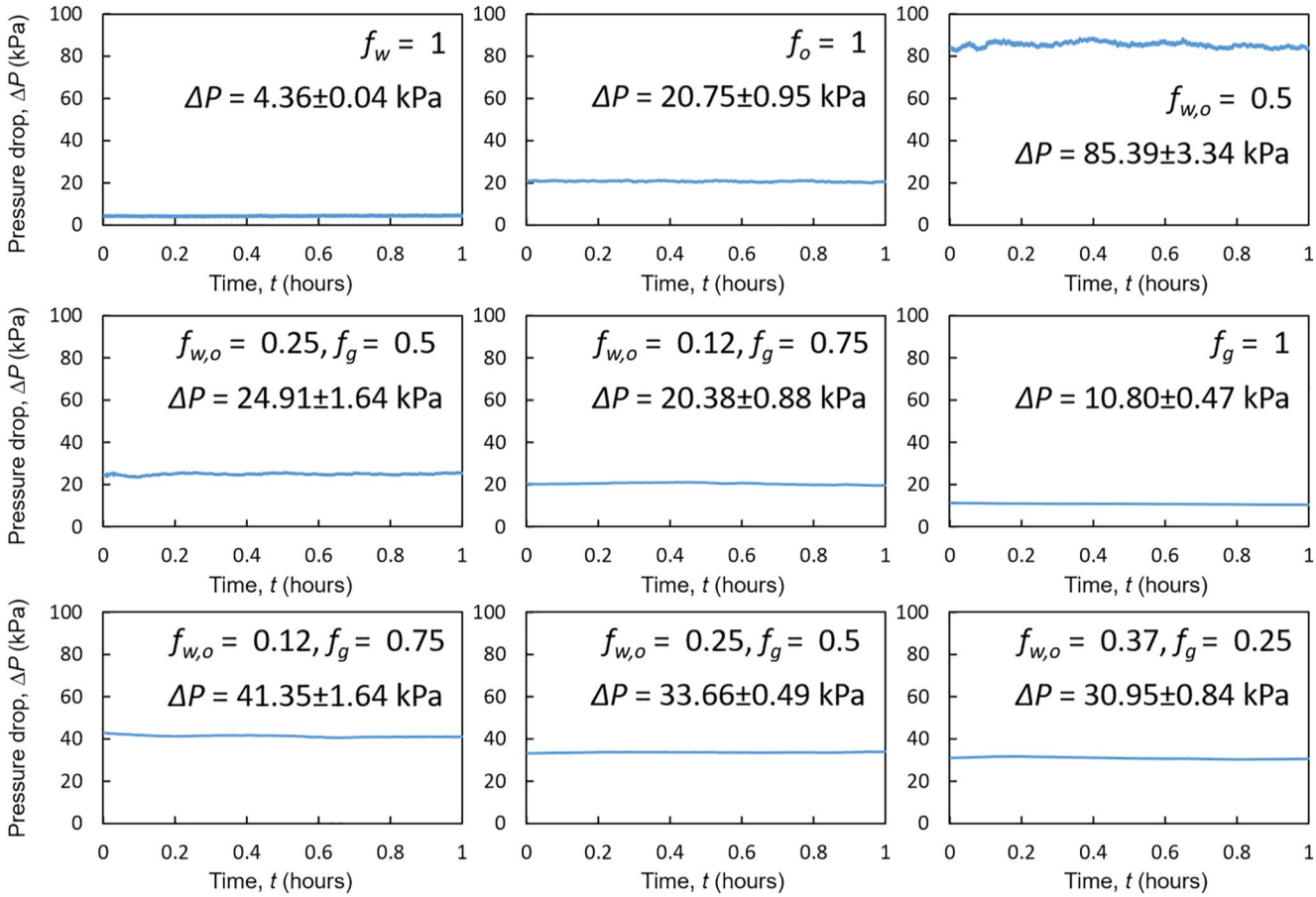

Figure 14. The measured pressure drops across the sample using a differential pressure transducer for 1 hr when steady-state conditions are reached at different fractional flows. Gas, oil and water fractional flows (f_g and $f_{w,o}$) are stated. The mean pressure drop values, with their corresponding standard deviations are shown.

to calculate the three-phase relative permeabilities, with their corresponding standard deviations. Increasing the gas flow rate decreased the pressure drop which is consistent with the introduction of a less viscous phase in the sample (Blunt, 2017). The pressure drop in the flow lines was insignificant compared to that measured across the sample and hence was ignored.

First, we compare our two-phase relative permeabilities, measured in flooding steps 1–3, see Table 1, with a two-phase relative permeability experiment conducted on a smaller water-wet Bentheimer sandstone sample of diameter 6.1 mm and length 25.8 mm (Lin et al., 2018, 2019). The two-phase relative permeabilities are shown in Figure S5. The results show that the measurements are in agreement, and the only discrepancy is at irreducible water saturation which is larger in our experiment, since we imposed a lower capillary pressure and the end of primary drainage.

Figure 15 shows the measured water, oil, and gas three-phase relative permeabilities at steady-state conditions. We compare our relative permeability with two three-phase relative permeability experiments, labeled as Exp A and Exp B, conducted by Alizadeh and Piri (2014a) on a larger sample of Bentheimer sandstone (3.81 cm in diameter and 15.24 cm in length). Figure 15 is divided into two columns: in the left column, are the relative permeabilities measured during the increasing f_g, and decreasing f_o and f_w, flow path, while on the right are the permeabilities of the decreasing f_g, and increasing f_o and f_w path. Note that Exp B only investigates the increasing f_g flow path.

The data set of Alizadeh and Piri (2014a) was chosen to validate our measurements against for a number of reasons: (a) the same rock type, Bentheimer sandstone, was used; (b) similar initial oil and water saturations (before gas injection); and (c) the same saturation path is investigated, first, increasing f_g, and decreasing f_o and

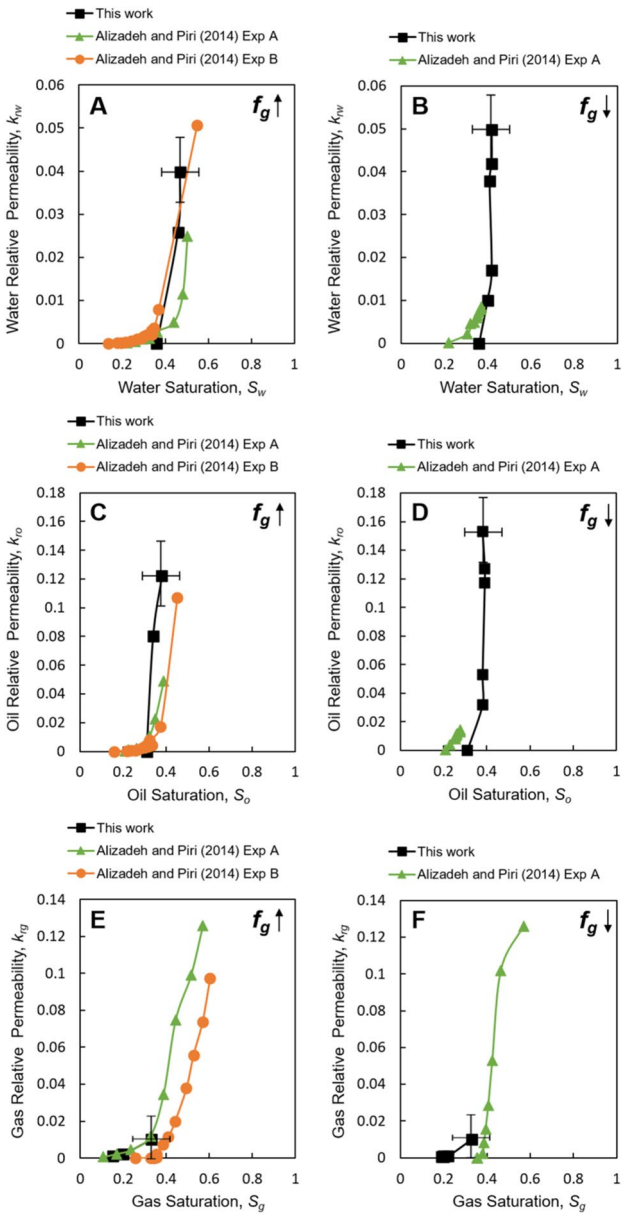

Figure 15. The measured three-phase relative permeability of (a) water, (c) oil, and (e) gas during increasing gas fractional flow, decreasing oil and water fractional flows, and of (b) water, (d) oil, and (f) gas during decreasing gas fractional flow, increasing oil and water. Exp A and Exp B data from Alizadeh and Piri (2014a). The upward and downward pointing arrows represent the saturation path where gas fractional flow (f_g) is increased and decreased respectively. Error bars indicate the uncertainty in the measurements.

f_w, and then decreasing f_g, and increasing f_o and f_w, with equal oil and water flow rates.

We observe that the water and oil relative permeabilities in our experiment, for increasing f_g, agree with the data of Alizadeh and Piri (2014a) which indicates the accuracy of our steady-state three-phase relative permeability measurement method. Furthermore, it shows that the sample size used in our experiment is well within the representative elementary volume (REV) for relative permeability, see Figures 15a and 15c. However, Figures 15b and 15d show that for decreasing f_g, the measured water and oil relative permeabilities are in a different saturation range compared to the data of Alizadeh and Piri (2014a). This is because they increased the gas flow rate at $f_g = 1$, which reduced the water and oil saturations in the pore space, while we did not. Hence our permeability measurements are at lower gas saturation compared to Alizadeh and Piri (2014a), see Figures 15e and 15f. However, we still see a match in the gas relative permeability at low gas saturations for increasing f_g, see Figure 15e.

Figure 15 shows that, in our experiment, the gas relative permeability is lower than the oil and water relative permeabilities, despite gas occupying the larger pores. This counter-intuitive behavior can be explained by the disconnected gas flow observed in Section 3.4. Although both oil and water flow in connected layers, the oil relative permeability is still higher than the water one, Figures 15a–15c, and 15d. This is attributed to oil flowing in medium-sized pores, while water flows in smaller pores and layers close to the solid surface.

Our results show that the saturation history has little impact on the water relative permeability, see Figure S6a. This is expected since water is the most wetting phase in the pore space. However, we observe a clear dependency of oil and gas relative permeabilities on the saturation history, see Figures S6b and S6c.

3.6. Intermittency in Three-Phase Flow

We observe that a significant fraction of the pore space is filled with two fluid phases during the scan time, identified by an intermediate gray-scale level, see Figure 16. This pore-scale phenomenon, called intermittency, has been seen hitherto in two-phase flow and refers to the alternative filling of the same pore by two immiscible fluid phases (Gao et al., 2017, 2019; Gao, Raeini, et al., 2020; Reynolds et al., 2017; Spurin et al., 2019a, 2019b).

In two-phase flow, intermittency has only been observed at moderate to high flow rates (Gao, Lin, et al., 2020), where the relationship between rate and pressure gradient is non-linear, far from the Darcy (capillary-dominated) regime. The onset of the transition from the Darcy regime to the non-linear behaviour was quantified by Zhang et al. (2021) using a pore-scale energy balance. We use their approach, assuming two-phase flow between gas and oil, and oil and water, see Figure S7. For oil-water displacement, the flow is clearly in the Darcy capillary-dominated regime, whereas for gas-oil flow, because of the lower gas viscosity, the experiments are on the predicted boundary between Darcy-like and intermittent flow. This suggests that the intermittent flow regions observed in our three-phase experiment can occur even under capillary-controlled flow conditions. Since gas, the most non-wetting phase, is disconnected in the pore space, it can only progress through the intermittent opening and closing of critical flow paths facilitated by double and multiple displacement events.

We identify two intermittent regions in the pore-scale images: (a) a more dominant gas-oil region, and (b) an oil-water region, see Figure 16. No intermittent gas-water flow was observed since the two phases do not directly

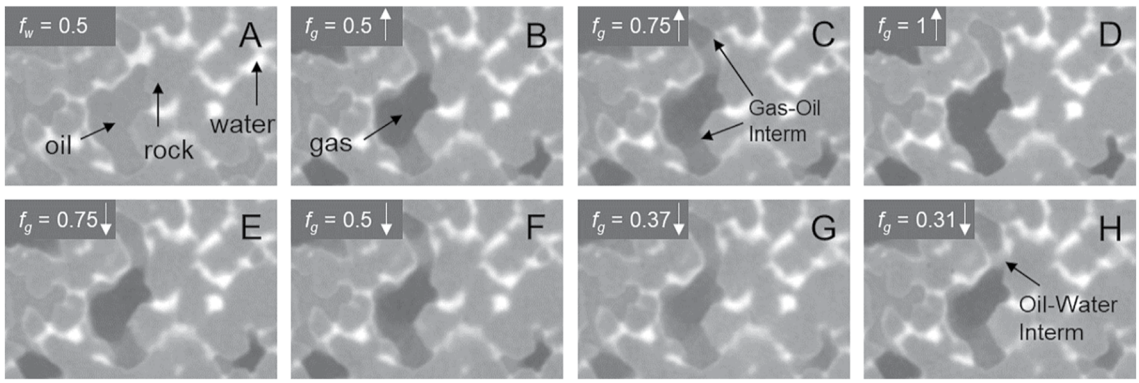

Figure 16. Two-dimensional unfiltered pore-scale images showing the occurrence of gas-oil and oil-water intermittency under three-phase flow conditions in the same pore at different fractional flows. The upward and downward pointing arrows represent the saturation path where gas fractional flow (f_g) is increased and decreased respectively. Water is shown in white, rock in light gray, oil in dark gray, and gas in black. Intermittency appears with with a gray-scale value that is in between the gray-scale values of the two intermittent phases.

contact each other in the pore space. In Figure 17, we quantify the intermittent gas-oil fraction of the pore space at different fractional flows and show that it occurs mostly in intermediate-sized pores, smaller than those occupied by gas, which indicates that gas forges temporary pathways to increases its conductance in the pore space.

3.7. Local Capillary Pressure

Using pore-scale imaging we were able to measure the local capillary pressures simultaneously with the steady-state three-phase relative permeability. Figure 18 shows the measured oil-water and gas-oil pressures using the curvature-based approach described in Section 2.5.2. Again, intermittency was not considered in this analysis; we do not expect this to influence the trend of capillary pressure change with saturation.

The two-phase oil-water capillary pressure is compared with the pressure measurements of Lin et al. (2019) obtained using two-phase flow imaging on a water-wet Bentheimer sandstone, see Figure 18a. The measured oil-water capillary pressures are in the same range (+2.5 kPa ± 0.4 kPa) demonstrating the consistency of the curvature-based approach. A positive oil-water capillary pressure indicates that the rock surfaces are indeed water-wet. There is little change in the oil-water capillary pressure with water saturation in both experiments; this is due to the relatively narrow pore size distribution of the Bentheimer sandstone, see Figure S1.

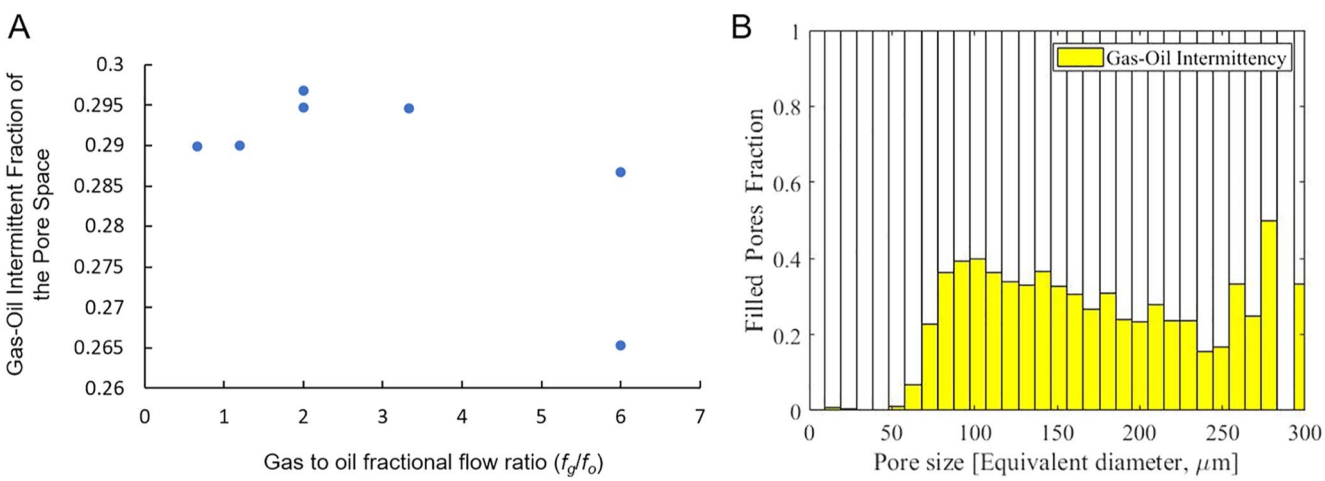

Figure 17. (a) Quantification of the fraction of the pore space occupied by gas-oil intermittency at different gas to oil fractional flow ratios. (b) A bar chart showing the pore occupancy of gas-oil intermittency at flooding step 5, see Table 1.

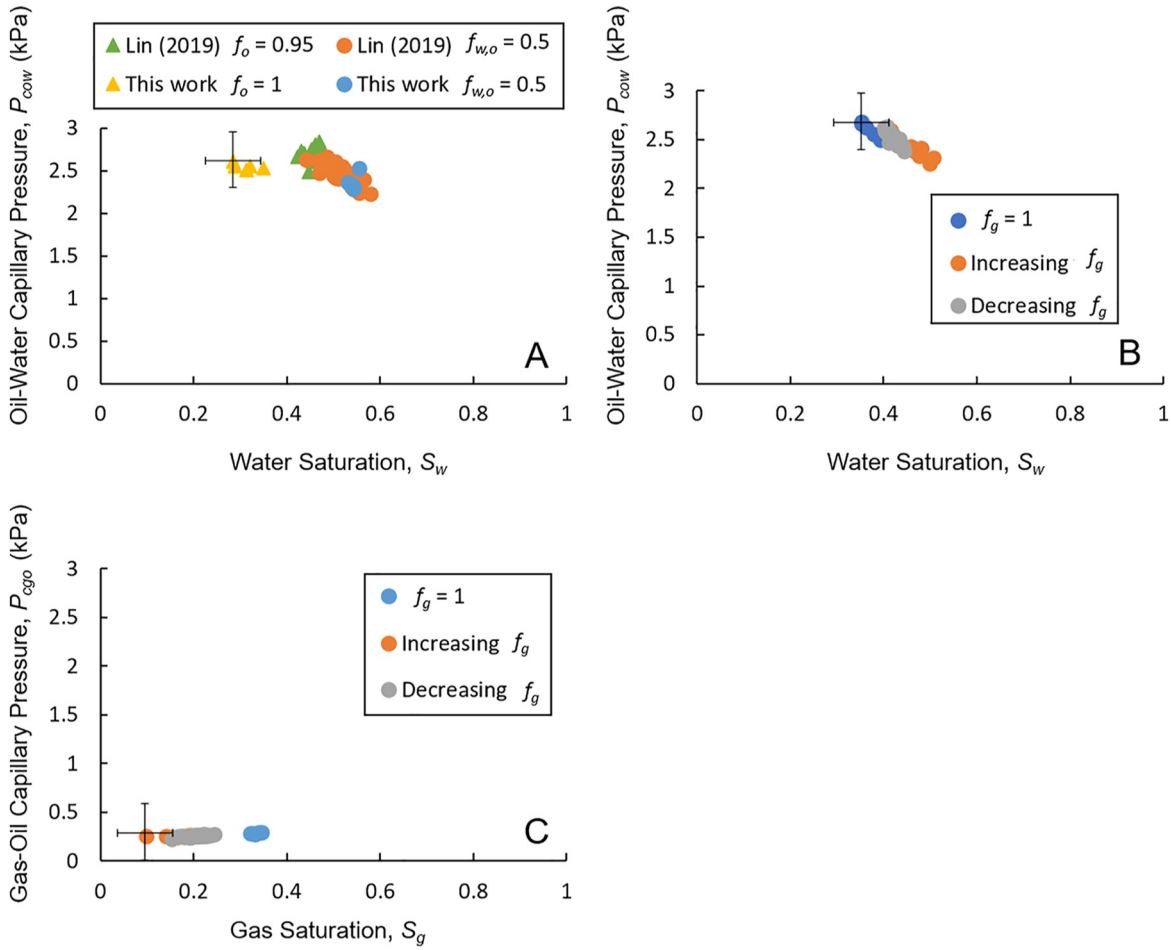

Figure 18. The curvature-based (a) two-phase oil-water, (b) three-phase oil-water, and (c) three-phase gas-oil capillary pressures plotted as a function of water and gas saturations. Increasing f_g represents the pressures obtained during the increasing gas fractional flow, decreasing oil and water fractional flows, saturation path, while decreasing f_g is of the decreasing gas fractional flow, increasing oil and water, path. The two-phase oil-water capillary pressures are compared to the measurements of Lin et al. (2019). Error bars indicate the uncertainty in the measurements.

Under three-phase flow conditions, Figure 18b, the oil-water capillary pressure decreased with increasing water saturation as expected. The gas-oil capillary pressure is also positive, with an average value of +0.26 kPa ± 0.4 kPa, indicating that oil is wetting to gas, see Figure 18c. This confirms the expected wettability order, water-oil-gas from most to least wetting, for the water-wet system at immiscible conditions. The gas-oil capillary pressure increased slightly with gas saturation. Again, it was not possible to measure the gas-water capillary pressure due to oil spreading layers preventing their contact in the pore space.

3.8. Double and Multiple Displacement

As gas exists in the form of disconnected ganglia, it can only propagate through the pore space by double and multiple displacement chains. These displacements will always involve oil as a mediator between gas and water as the two phases do not contact each other in the pore space.

Two double displacement processes were observed in the steady-state pore-scale images: (a) a gas-oil-water double displacement and (b) a water-oil-gas displacement, see Figure 19. The same double displacements were previously observed in water-wet unsteady-state experiments (Alhosani, Bijeljic, & Blunt, 2021; Øren et al., 1992; Scanziani, Singh, et al., 2018; Sohrabi et al., 2004). Figure 19a shows images of a gas-oil-water double displacement process in a single pore. Water was first displaced by oil in a drainage process which was then displaced by gas in another drainage process. Notice that during a gas-oil-water double displacement, gas does not completely

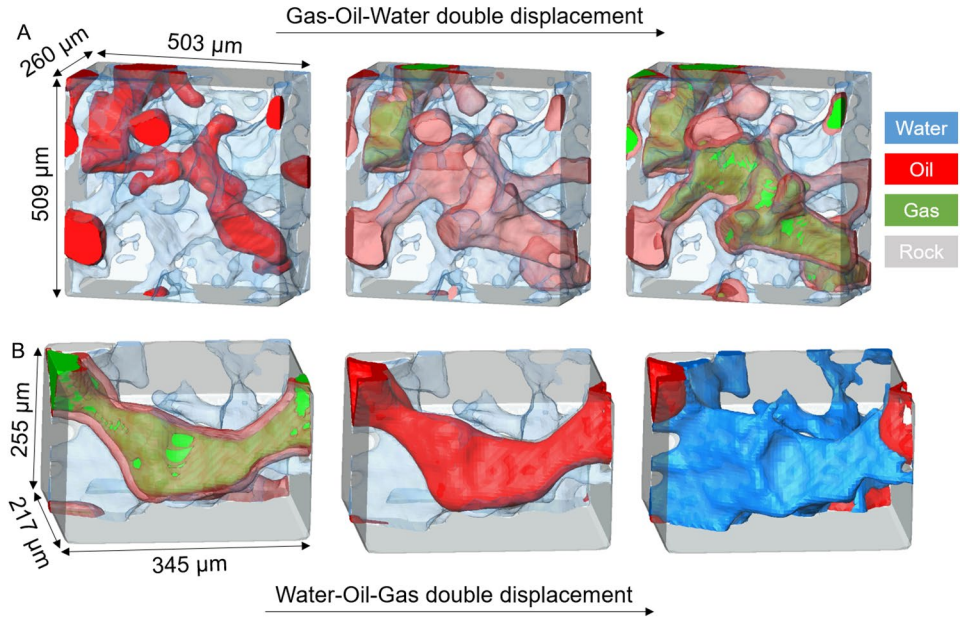

Figure 19. Three-dimensional images showing the occurrence of (a) gas-oil-water double displacement, and (b) water-oil-gas double displacement in the water-wet rock under capillary-dominated conditions. Water is shown in blue, oil in red, gas in green, while the rock phase is rendered semi-transparent (gray).

displace oil and water out of the pore space; oil and water remain connected in spreading and wetting layers respectively. However, during a water-oil-gas displacement, where oil first displaces gas in an imbibition process followed by another imbibition process when oil is displaced by water, the displaced phases completely exit the pore space; there is no remaining oil and gas, see Figure 19b.

4. Conclusions

We have developed a methodology to couple steady-state three-phase relative permeability measurements with high-resolution pore-scale X-ray imaging (5.3 µm per voxel). Three-phase relative permeability was determined simultaneously with capillary pressure at different gas, oil, and water fractional flows in a water-wet sandstone rock under capillary dominated conditions. In our water-wet system, at immiscible conditions, water is the most wetting phase, residing in small pores and wetting layers, gas is the most non-wetting phase, occupying the large pores, while oil is the intermediate-wet phase, forming spreading layers in the medium-sized pores. Combining macroscopic measurements of flow properties with pore-scale imaging allowed the following discoveries to be made:

1. Disconnected gas flow at steady-state conditions: We observed a unique gas flow pattern at steady-state conditions, where gas advances through the pore space in the form of disconnected ganglia mediated by double and multiple displacement processes. This behavior was attributed to the continuous swelling of water and oil layers in the throats, trapping gas in the pore centers. Gas was only connected in the pore space when injected at a gas fractional flow of one.
2. Intermittent flow: We identified intermittent gas-oil and gas-water regions, where both phases interchangeably occupied the same pores during the scan time. Gas-oil intermittency was more dominant. No gas-water intermittency was observed because the direct contact of the two phases is prevented by oil spreading layers. This intermittency is similar to that observed at moderate to high flow rates in two-phase flow but is observed in three-phase flow even under capillary-dominated displacement conditions. The periodic opening and closing of flow paths to gas facilitates its flow: gas ganglia are not advected through the pore space, but undergo a stop-start type transport, akin to cars controlled by traffic lights.
3. High residual gas saturation: A high residual gas saturation was observed in the flooding experiment; once gas invaded the pore space, it was not possible to displace it, when water and oil fractional flows were subsequently increased. This is due to double capillary trapping, where gas is trapped in the center of the pores

by oil and water layers; when more water and oil are injected, they imbibe in the corners of the pore space surrounding the gas phase in the centers, keeping it trapped. This has huge implications for gas storage applications in water-wet oil reservoirs, as it ensures that once gas is injected it remains trapped and does not flow once injection ceases.

4. Understanding three-phase relative permeability: The low gas relative permeability seen in water-wet systems, albeit occupying the largest pores, can now be attributed to disconnected gas flow. Even though both water and oil exist in layers, oil has higher relative permeability, which is ascribed to water occupying smaller pores than oil. The impact of saturation history on gas and oil relative permeabilities was larger than its impact on the water relative permeability. Our relative permeability results were in agreement with core-scale three-phase relative permeability measurements indicating the accuracy of our method.
5. Capillary pressures: The capillary pressure measurements displayed a positive oil-water and gas-oil capillary pressures consistent with a wettability order of water-oil-gas, from most to least wetting.
6. Double displacements in steady-state flow: Two double displacement processes were observed: (a) gas-oil-water, and (b) water-oil-gas. The latter is essential for gas to progress through the pore space since it exists in disconnected ganglia. During a gas-oil-water double displacement, oil and water remain connected in the corners of the invaded pore, while no residual gas and oil phases are left during a water-oil-gas displacement.

This analysis uncovers several topics for future work. (a) We need to quantify the apparent relative permeability for different flow rates. Is there a linear relationship between flow rate and pressure gradient and for what range of capillary number? (b) The analysis could be extended to mixed-wet and oil-wet rocks, and for a wider range of rock types. (c) The implications for modeling need to be explored. It is evident that the current quasi-static assumption of pore network models that compute relative permeability based on the connected network of each phase through the pore space is flawed. For empirical models that use two-phase analogies to predict three-phase properties, again the predictions are likely to be significantly in error since they do not encapsulate the unique nature of three-phase flow.

Data Availability Statement

The data acquired in this work are available online on the Digital Rocks Portal: https://doi.org/10.17612/g5m1-qy82.

Acknowledgment
The authors acknowledge Abu Dhabi National Oil Company (ADNOC) for the financial support.

References

Abdulkareem, F. A., & Padmanabhan, E. (2021). Applied techniques for residual oil recovery from source rocks: A review of current challenges and possible developments. *Canadian Journal of Chemical Engineering*, *99*(1), 251–267. https://doi.org/10.1002/cjce.23838

Akai, T., Lin, Q., Alhosani, A., Bijeljic, B., & Blunt, J. M. (2019). Quantification of uncertainty and best practice in computing interfacial curvature from complex pore space images. *Materials*, *12*(13), 2138. https://doi.org/10.3390/ma12132138

Alhammadi, A. M., AlRatrout, A., Singh, K., Bijeljic, B., & Blunt, M. J. (2017). In situ characterization of mixed-wettability in a reservoir rock at subsurface conditions. *Scientific Reports*, *7*(1), 10753. https://doi.org/10.1038/s41598-017-10992-w

Alhammadi, A. M., Gao, Y., Akai, T., Blunt, M. J., & Bijeljic, B. (2020). Pore-scale X-ray imaging with measurement of relative permeability, capillary pressure and oil recovery in a mixed-wet micro-porous carbonate reservoir rock. *Fuel*, *268*, 117018. https://doi.org/10.1016/j.fuel.2020.117018

Alhosani, A., Bijeljic, B., & Blunt, M. J. (2021). Pore-scale imaging and analysis of wettability order, trapping and displacement in three-phase flow in porous media with various wettabilities. *Transport in Porous Media*, *140*, 59–84. https://doi.org/10.1007/s11242-021-01595-1

Alhosani, A., Lin, Q., Scanziani, A., Andrews, E., Zhang, K., Bijeljic, B., & Blunt, M. J. (2021). Pore-scale characterization of carbon dioxide storage at immiscible and near-miscible conditions in altered-wettability reservoir rocks. *International Journal of Greenhouse Gas Control*, *105*, 103232. https://doi.org/10.1016/j.ijggc.2020.103232

Alhosani, A., Scanziani, A., Lin, Q., Foroughi, S., Alhammadi, A. M., Blunt, M. J., & Bijeljic, B. (2020). Dynamics of water injection in an oil-wet reservoir rock at subsurface conditions: Invasion patterns and pore-filling events. *Physical Review E*, *102*(2), 023110. https://doi.org/10.1103/PhysRevE.102.023110

Alhosani, A., Scanziani, A., Lin, Q., Pan, Z., Bijeljic, B., & Blunt, M. J. (2019). In situ pore-scale analysis of oil recovery during three-phase near-miscible CO_2 injection in a water-wet carbonate rock. *Advances in Water Resources*, *134*, 103432. https://doi.org/10.1016/j.advwatres.2019.103432

Alhosani, A., Scanziani, A., Lin, Q., Raeini, A. Q., Bijeljic, B., & Blunt, M. J. (2020). Pore-scale mechanisms of CO_2 storage in oilfields. *Scientific Reports*, *10*(1), 8534. https://doi.org/10.1038/s41598-020-65416-z

Alhosani, A., Scanziani, A., Lin, Q., Selem, A., Pan, Z., Blunt, M. J., & Bijeljic, B. (2020). Three-phase flow displacement dynamics and Haines jumps in a hydrophobic porous medium. *Proceedings of the Royal Society A: Mathematical, Physical & Engineering Sciences*, *476*(2244), 20200671. https://doi.org/10.1098/rspa.2020.0671

Alizadeh, A., & Piri, M. (2014a). The effect of saturation history on three–phase relative permeability. *An experimental study*, *50*(2), 1636–1664. https://doi.org/10.1002/2013wr014914

Alizadeh, A. H., & Piri, M. (2014b). Three-phase flow in porous media: A review of experimental studies on relative permeability. *Reviews of Geophysics*, *52*(3), 468–521. https://doi.org/10.1002/2013RG000433

AlRatrout, A., Raeini, A. Q., Bijeljic, B., & Blunt, M. J. (2017). Automatic measurement of contact angle in pore-space images. *Advances in Water Resources*, *109*, 158–169. https://doi.org/10.1016/j.advwatres.2017.07.018

Andrew, M., Bijeljic, B., & Blunt, M. J. (2014a). Pore-by-pore capillary pressure measurements using X-ray microtomography at reservoir conditions: Curvature, snap-off, and remobilization of residual CO_2. *Water Resources Research*, *50*(11), 8760–8774. https://doi.org/10.1002/2014WR015970

Andrew, M., Bijeljic, B., & Blunt, M. J. (2014b). Pore-scale contact angle measurements at reservoir conditions using X-ray microtomography. *Advances in Water Resources*, *68*, 24–31. https://doi.org/10.1016/j.advwatres.2014.02.014

Andrew, M., Bijeljic, B., & Blunt, M. J. (2014c). Pore-scale imaging of trapped supercritical carbon dioxide in sandstones and carbonates. *International Journal of Greenhouse Gas Control*, *22*, 1–14. https://doi.org/10.1016/j.ijggc.2013.12.018

Armstrong, R. T., Porter, M. L., & Wildenschild, D. (2012). Linking pore-scale interfacial curvature to column-scale capillary pressure. *Advances in Water Resources*, *46*, 55–62. https://doi.org/10.1016/j.advwatres.2012.05.009

Baker, L. E. (1988). *Three-phase relative permeability correlations*. https://doi.org/10.2118/17369-MS

Berg, S., Ott, H., Klapp, S. A., Schwing, A., Neiteler, R., Brussee, N., et al. (2013). Real-time 3D imaging of Haines jumps in porous media flow. *Proceedings of the National Academy of Sciences*, *110*(10), 3755–3759. https://doi.org/10.1073/pnas.1221373110

Bickle, M. J. (2009). Geological carbon storage. *Nature Geoscience*, *2*(12), 815–818. https://doi.org/10.1038/ngeo687

Blunt, M., Fayers, F. J., & Orr, F. M. (1993). Carbon dioxide in enhanced oil recovery. *Energy Conversion and Management*, *34*(9), 1197–1204. https://doi.org/10.1016/0196-8904(93)90069-M

Blunt, M. J. (2017). *Multiphase flow in permeable media: A pore-scale perspective*. Cambridge University Press.

Blunt, M. J., Alhosani, A., Lin, Q., Scanziani, A., & Bijeljic, B. (2021). Determination of contact angles for three-phase flow in porous media using an energy balance. *Journal of Colloid and Interface Science*, *582*, 283–290. https://doi.org/10.1016/j.jcis.2020.07.152

Blunt, M. J., Bijeljic, B., Dong, H., Gharbi, O., Iglauer, S., Mostaghimi, P., et al. (2013). Pore-scale imaging and modelling. *Advances in Water Resources*, *51*, 197–216. https://doi.org/10.1016/j.advwatres.2012.03.003

Bultreys, T., Van Hoorebeke, L., & Cnudde, V. (2015). Multi-scale, micro-computed tomography-based pore network models to simulate drainage in heterogeneous rocks. *Advances in Water Resources*, *78*, 36–49. https://doi.org/10.1016/j.advwatres.2015.02.003

Cnudde, V., & Boone, M. N. (2013). High-resolution X-ray computed tomography in geosciences: A review of the current technology and applications. *Earth-Science Reviews*, *123*, 1–17. https://doi.org/10.1016/j.earscirev.2013.04.003

Descorme, C. (2017). Catalytic wastewater treatment: Oxidation and reduction processes. Recent studies on chlorophenols. *Catalysis Today*, *297*, 324–334. https://doi.org/10.1016/j.cattod.2017.03.039

Dong, H., & Blunt, M. J. (2009). Pore-network extraction from micro-computerized-tomography images. *Physical Review E*, *80*(3), 036307. https://doi.org/10.1103/PhysRevE.80.036307

Feali, M., Pinczewski, W., Cinar, Y., Arns, C. H., Arns, J.-Y., Francois, N., et al. (2012). Qualitative and quantitative analyses of the three-phase distribution of oil, water, and gas in Bentheimer sandstone by use of micro-CT imaging. *SPE Reservoir Evaluation and Engineering*, *15*(06), 706–711. https://doi.org/10.2118/151609-PA

Gao, Y., Lin, Q., Bijeljic, B., & Blunt, M. J. (2017). X-ray microtomography of intermittency in multiphase flow at steady state using a differential imaging method. *Water Resources Research*, *53*(12), 10274–10292. https://doi.org/10.1002/2017WR021736

Gao, Y., Lin, Q., Bijeljic, B., & Blunt, M. J. (2020). Pore-scale dynamics and the multiphase Darcy law. *Physical Review Fluids*, *5*(1), 013801. https://doi.org/10.1103/PhysRevFluids.5.013801

Gao, Y., Qaseminejad Raeini, A., Blunt, M. J., & Bijeljic, B. (2019). Pore occupancy, relative permeability and flow intermittency measurements using X-ray micro-tomography in a complex carbonate. *Advances in Water Resources*, *129*, 56–69. https://doi.org/10.1016/j.advwatres.2019.04.007

Gao, Y., Raeini, A. Q., Selem, A. M., Bondino, I., Blunt, M. J., & Bijeljic, B. (2020). Pore-scale imaging with measurement of relative permeability and capillary pressure on the same reservoir sandstone sample under water-wet and mixed-wet conditions. *Advances in Water Resources*, *146*, 103786. https://doi.org/10.1016/j.advwatres.2020.103786

Gjennestad, M. A., Winkler, M., & Hansen, A. (2020). Pore network modeling of the effects of viscosity ratio and pressure gradient on steady-state incompressible two-phase flow in porous media. *Transport in Porous Media*, *132*(2), 355–379. https://doi.org/10.1007/s11242-020-01395-z

Herring, A. L., Andersson, L., Schlüter, S., Sheppard, A., & Wildenschild, D. (2015). Efficiently engineering pore-scale processes: The role of force dominance and topology during nonwetting phase trapping in porous media. *Advances in Water Resources*, *79*, 91–102. https://doi.org/10.1016/j.advwatres.2015.02.005

Herring, A. L., Harper, E. J., Andersson, L., Sheppard, A., Bay, B. K., & Wildenschild, D. (2013). Effect of fluid topology on residual nonwetting phase trapping: Implications for geologic CO_2 sequestration. *Advances in Water Resources*, *62*, 47–58. https://doi.org/10.1016/j.advwatres.2013.09.015

Herring, A. L., Middleton, J., Walsh, R., Kingston, A., & Sheppard, A. (2017). Flow rate impacts on capillary pressure and interface curvature of connected and disconnected fluid phases during multiphase flow in sandstone. *Advances in Water Resources*, *107*, 460–469. https://doi.org/10.1016/j.advwatres.2017.05.011

Herring, A. L., Robins, V., & Sheppard, A. P. (2019). Topological persistence for relating microstructure and capillary fluid trapping in sandstones. *Water Resources Research*, *55*(1), 555–573. https://doi.org/10.1029/2018WR022780

Honarpour, M. M., Koederitz, F., & Herbert, A. (1986). *Relative permeability of petroleum reservoirs*. CRC Press Inc, Boca Raton, FL.

Iglauer, S., Paluszny, A., Rahman, T., Zhang, Y., Wülling, W., & Lebedev, M. (2019). Residual trapping of CO_2 in an oil-filled, oil-wet sandstone core: Results of three-phase pore-scale imaging. *Geophysical Research Letters*, *46*(20), 11146–11154. https://doi.org/10.1029/2019GL083401

Jianhua, T. (1993). Density and interfacial tension of nitrogen-hydrocarbon systems at elevated pressures. 中国化学工程学报, *1*(4), 223–231.

Kramer, D. (2020). Negative carbon dioxide emissions. *Physics Today*, *73*(1), 44–51. https://doi.org/10.1063/pt.3.4389

Lake, L. W. (1989). *Enhanced oil recovery*.

Lin, Q., Al-Khulaifi, Y., Blunt, M. J., & Bijeljic, B. (2016). Quantification of sub-resolution porosity in carbonate rocks by applying high-salinity contrast brine using X-ray microtomography differential imaging. *Advances in Water Resources*, *96*, 306–322. https://doi.org/10.1016/j.advwatres.2016.08.002

Lin, Q., Bijeljic, B., Berg, S., Pini, R., Blunt, M. J., & Krevor, S. (2019). Minimal surfaces in porous media: Pore-scale imaging of multiphase flow in an altered-wettability Bentheimer sandstone. *Physical Review E*, *99*(6), 063105. https://doi.org/10.1103/PhysRevE.99.063105

Lin, Q., Bijeljic, B., Pini, R., Blunt, M. J., & Krevor, S. (2018). Imaging and measurement of pore-scale interfacial curvature to determine capillary pressure simultaneously with relative permeability. *Water Resources Research*, *54*(9), 7046–7060. https://doi.org/10.1029/2018WR023214

Mayer, A. S., & Miller, C. T. (1993). An experimental investigation of pore-scale distributions of nonaqueous phase liquids at residual saturation. *Transport in Porous Media*, *10*(1), 57–80. https://doi.org/10.1007/BF00617511

Mecke, K. R., & Wagner, H. (1991). Euler characteristic and related measures for random geometric sets. *Journal of Statistical Physics*, *64*(3), 843–850. https://doi.org/10.1007/BF01048319

NIST. (2019). *Reference fluid thermodynamic and transport properties database (REFPROP)*. Retrieved from https://www.nist.gov/srd/refprop

Oak, M. J. (1990). Three-phase relative permeability of water-wet Berea. In *Paper presented at the SPE/DOE enhanced oil recovery symposium*. https://doi.org/10.2118/20183-MS

Oak, M. J., Baker, L. E., & Thomas, D. C. (1990). Three-phase relative permeability of Berea sandstone. *Journal of Petroleum Technology*, *42*(08), 1054–1061. https://doi.org/10.2118/17370-PA

Øren, P. E., Billiotte, J., & Pinczewski, W. V. (1992). Mobilization of Waterflood Residual Oil by Gas Injection for Water-Wet Conditions. *SPE Formation Evaluation*, *7*(01), 70–78. https://doi.org/10.2118/20185-PA

Peksa, A. E., Wolf, K.-H. A. A., & Zitha, P. L. J. (2015). Bentheimer sandstone revisited for experimental purposes. *Marine and Petroleum Geology*, *67*, 701–719. https://doi.org/10.1016/j.marpetgeo.2015.06.001

Piri, M., & Blunt, M. J. (2005a). Three-dimensional mixed-wet random pore-scale network modeling of two- and three-phase flow in porous media. I. Model description. *Physical Review E*, *71*(2), 026301. https://doi.org/10.1103/PhysRevE.71.026301

Piri, M., & Blunt, M. J. (2005b). Three-dimensional mixed-wet random pore-scale network modeling of two- and three-phase flow in porous media. II. Results. *Physical Review E*, *71*(2), 026302. https://doi.org/10.1103/PhysRevE.71.026302

Qin, Z., Arshadi, M., & Piri, M. (2019). Micro-scale experimental investigations of multiphase flow in oil-wet carbonates. II. Tertiary gas injection and WAG. *Fuel*, *257*, 116012. https://doi.org/10.1016/j.fuel.2019.116012

Raeini, A. Q., Bijeljic, B., & Blunt, M. J. (2017). Generalized network modeling: Network extraction as a coarse-scale discretization of the void space of porous media. *Physical Review E*, *96*(1), 013312. https://doi.org/10.1103/PhysRevE.96.013312

Reynolds, C. A., Menke, H., Andrew, M., Blunt, M. J., & Krevor, S. (2017). Dynamic fluid connectivity during steady-state multiphase flow in a sandstone. *Proceedings of the National Academy of Sciences*, *114*(31), 8187–8192. https://doi.org/10.1073/pnas.1702834114

Salathiel, R. A. (1973). Oil recovery by surface film drainage in mixed-wettability rocks. *Journal of Petroleum Technology*, *25*(10), 1216–1224. https://doi.org/10.2118/4104-PA

Saraf, D. N., Batycky, J. P., Jackson, C. H., & Fisher, D. B. (1982). An experimental investigation of three-phase flow of water-oil- gas mixtures through water-wet sandstones. *Paper presented at the SPE California regional meeting*. https://doi.org/10.2118/10761-MS

Scanziani, A., Alhammadi, A., Bijeljic, B., & Blunt, M. J. (2018). Three-phase flow visualization and characterization for a mixed-wet carbonate rock. In *Paper presented at the Abu Dhabi international petroleum exhibition & conference*. https://doi.org/10.2118/192666-MS

Scanziani, A., Alhosani, A., Lin, Q., Spurin, C., Garfi, G., Blunt, M. J., & Bijeljic, B. (2020). In situ characterization of three-phase flow in mixed-wet porous media using synchrotron imaging. *Water Resources Research*, *56*(9), e2020WR027873. https://doi.org/10.1029/2020WR027873

Scanziani, A., Lin, Q., Alhosani, A., Blunt, M. J., & Bijeljic, B. (2020). Dynamics of fluid displacement in mixed-wet porous media. *Proceedings of the Royal Society A: Mathematical, Physical & Engineering Sciences*, *476*(2240), 20200040. https://doi.org/10.1098/rspa.2020.0040

Scanziani, A., Singh, K., Bultreys, T., Bijeljic, B., & Blunt, M. J. (2018). In situ characterization of immiscible three-phase flow at the pore scale for a water-wet carbonate rock. *Advances in Water Resources*, *121*, 446–455. https://doi.org/10.1016/j.advwatres.2018.09.010

Scanziani, A., Singh, K., Menke, H., Bijeljic, B., & Blunt, M. J. (2019). Dynamics of enhanced gas trapping applied to CO_2 storage in the presence of oil using synchrotron X-ray micro tomography. *Applied Energy*, *259*, 114136. https://doi.org/10.1016/j.apenergy.2019.114136

Singh, K., Bijeljic, B., & Blunt, M. J. (2016). Imaging of oil layers, curvature and contact angle in a mixed-wet and a water-wet carbonate rock. *Water Resources Research*, *52*(3), 1716–1728. https://doi.org/10.1002/2015WR018072

Singh, K., Menke, H., Andrew, M., Lin, Q., Rau, C., Blunt, M. J., & Bijeljic, B. (2017). Dynamics of snap-off and pore-filling events during two-phase fluid flow in permeable media. *Scientific Reports*, *7*(1), 5192. https://doi.org/10.1038/s41598-017-05204-4

Sohrabi, M., Tehrani, D. H., Danesh, A., & Henderson, G. D. (2004). Visualization of Oil Recovery by Water-Alternating-Gas Injection Using High-Pressure Micromodels. *SPE Journal*, *9*(03), 290–301. https://doi.org/10.2118/89000-PA

Sorbie, K. S., & van Dijke, M. I. (2010). *The mechanism of oil recovery by water-alternating-gas injection at near-miscible conditions in mixed wet systems*. https://doi.org/10.2118/129837-MS

Spurin, C., Bultreys, T., Bijeljic, B., Blunt, M. J., & Krevor, S. (2019a). Intermittent fluid connectivity during two-phase flow in a heterogeneous carbonate rock. *Physical Review E*, *100*(4), 043103. https://doi.org/10.1103/PhysRevE.100.043103

Spurin, C., Bultreys, T., Bijeljic, B., Blunt, M. J., & Krevor, S. (2019b). Mechanisms controlling fluid breakup and reconnection during two-phase flow in porous media. *Physical Review E*, *100*(4), 043115. https://doi.org/10.1103/PhysRevE.100.043115

Stewart, R. J., Johnson, G., Heinemann, N., Wilkinson, M., & Haszeldine, R. S. (2018). Low carbon oil production: Enhanced oil recovery with CO_2 from North Sea residual oil zones. *International Journal of Greenhouse Gas Control*, *75*, 235–242. https://doi.org/10.1016/j.ijggc.2018.06.009

Stone, H. L. (1970). Probability model for estimating three-phase relative permeability. *Journal of Petroleum Technology*, *22*(02), 214–218. https://doi.org/10.2118/2116-PA

ToolBox, E. (2018). *Nitrogen - dynamic and kinematic viscosity*. Retrieved from https://www.engineeringtoolbox.com/nitrogen-N2-dynamic-kinematic-viscosity-temperature-pressure-d_2067.html

van Dijke, M. I. J., & Sorbie, K. S. (2002). An analysis of three-phase pore occupancies and relative permeabilities in porous media with variable wettability. *Transport in Porous Media*, *48*(2), 159–185. https://doi.org/10.1023/A:1015692630733

Vogel, H.-J. (2002). Topological characterization of porous media. In K. Mecke, & D. Stoyan (Eds.), *Morphology of condensed matter: Physics and geometry of spatially complex systems* (pp. 75–92). Berlin, Heidelberg. Springer Berlin Heidelberg. https://doi.org/10.1007/3-540-45782-8_3

Vogel, H. J., & Kretzschmar, A. (1996). Topological characterization of pore space in soil — sample preparation and digital image-processing. *Geoderma*, *73*(1), 23–38. https://doi.org/10.1016/0016-7061(96)00043-2

Wildenschild, D., & Sheppard, A. P. (2013). X-ray imaging and analysis techniques for quantifying pore-scale structure and processes in subsurface porous medium systems. *Advances in Water Resources*, *51*, 217–246. https://doi.org/10.1016/j.advwatres.2012.07.018

Wyckoff, R. D., & Botset, H. G. (1936). The flow of gas-liquid mixtures through unconsolidated sands. *Physics*, *7*(9), 325–345. https://doi.org/10.1063/1.1745402

Zhang, Y., Bijeljic, B., Gao, Y., Lin, Q., & Blunt, M. J. (2021). Quantification of nonlinear multiphase flow in porous media. *Geophysical Research Letters*, *48*(5), e2020GL090477. https://doi.org/10.1029/2020GL090477

Zou, S., Armstrong, R. T., Arns, J.-Y., Arns, C. H., & Hussain, F. (2018). Experimental and theoretical evidence for increased ganglion dynamics during fractional flow in mixed-wet porous media. *Water Resources Research*, *54*(5), 3277–3289. https://doi.org/10.1029/2017WR022433